

A Robust Launching Mechanism for Freely-Floating Planets from Host Stars with Close-in Planets

XIAOCHEN ZHENG (郑晓晨) ,¹ ZHUoya CAO (曹卓雅) ,^{2,3} SHIGERU IDA (井田茂) ,^{4,2}
 DOUGLAS N.C. LIN (林潮) ,^{5,2} AND SHUDE MAO (毛淑德) ²

¹ Beijing Planetarium, Beijing, 100044, China

² Department of Astronomy, Westlake University, Hangzhou 310030, Zhejiang Province, China

³ Department of Astronomy, Tsinghua University, Beijing, 100084, China

⁴ Earth and Life Science Institute, Institute of Science, Meguro, Tokyo, 152-8550, Japan

⁵ Department of Astronomy and Astrophysics, University of California, Santa Cruz, CA 95064, USA

ABSTRACT

Secular perturbations from binary stars and distant massive planets can drive cold planets onto nearly parabolic orbits with pericenter passages extremely close to their host stars. Meanwhile, short-period super-Earths are frequently observed around nearby stars. Gravitational scattering between these two distinct populations can lead to substantial orbital energy exchange, liberating some intruders from the gravitational confinement of their host systems. This process offers a robust formation channel for a subset of the abundant freely floating planet population. It may also significantly perturb the original orbits of close-in planets, induce collisional trajectories between close-in planets and their host stars, and disrupt the dynamical evolution of cold planets toward close stellar encounters.

Keywords: methods: analytical — methods: numerical — planet–star interactions — planets and satellites: dynamical evolution and stability — planets and satellites: general

1. INTRODUCTION

Over the past three decades, significant advancements in exoplanet detection techniques and methods have led to the confirmation of over 6,000 exoplanets (NASA Exoplanet Archive), with numerous additional candidates under investigation. This extensive sample has greatly enhanced our understanding of exoplanet demographics and planetary system architectures.

The demographic census of exoplanets is conducted through various detection methods, each subject to observational selection biases (Perryman 2018; Zhu & Dong 2021a). Among these populations, close-in planets are considerably more abundant. This category includes all planets with $P < 400$ days (Zhu & Dong 2021b), encompassing close-in Jupiters, super-Earths, and terrestrial planets. Most reside in multi-planet systems (Fabrycky et al. 2014), typically exhibiting low eccentricities and nearly coplanar orbits, with some of them in or near mean-motion resonances (Dai et al. 2024).

Occurrence rates show substantial variation across studies. Early HARPS data suggested 30–50% of GK-type stars host planets with minimum masses of $3\text{--}30 M_{\oplus}$ and orbital periods $P < 50$ days (Mayor et al. 2009; Mayor 2010), while Howard et al. (2010) found a rate of $\sim 15\%$ for similar parameters and predicted 23% of stars harbor smaller planets ($0.5\text{--}2 M_{\oplus}$). Subsequent work (Howard et al. 2012) reported occurrence rates of ~ 0.13 , ~ 0.023 , and ~ 0.013 planets per star for radius ranges of $2\text{--}4 R_{\oplus}$, $4\text{--}8 R_{\oplus}$, and $8\text{--}32 R_{\oplus}$, respectively, for $P < 50$ days.

Beyond this period, occurrence rates increase with orbital distance. Dong & Zhu (2013) found rates of $\sim 28\%$ (Earth-size), $\sim 25\%$ (super-Earths), $\sim 7\%$ (Neptune-size), and $\sim 3\%$ (Jupiter-size) within 250 days. The overall occurrence rate for giant planets within 400 days is $\sim 4.6\%$ (Santerne et al. 2016), with Jovian planets ($> 0.3 M_{\mathrm{J}}$)

beyond 100 days occurring at $\sim 6.7\%$ (Wittenmyer et al. 2020). These results collectively indicate a rising occurrence rate with orbital distance out to 1 au, consistent with *Kepler* statistics.

Long-period planets are primarily detected through direct imaging of young, luminous planets (Galicher et al. 2016) or inference from microlensing events (Gould et al. 2010). Due to the sensitivity limitations of these techniques, most known long-period planets are relatively massive. These distant giants are expected to play a disproportionately important role in shaping the dynamical evolution and kinematic architecture of planetary systems. This hypothesis is supported by observational evidence showing that systems containing long-period planets exhibit significantly more diverse orbital eccentricities compared to their compact counterparts.

In addition to bound planets, a vast population of free-floating planets (FFPs) has been revealed through microlensing surveys. The initial evidence emerged from short-duration events (1–2 days), which Sumi et al. (2011) attributed to a substantial population of unbound or wide-orbit Jupiter-mass planets, although such a population was found difficult to reproduce from population synthesis models (Ma et al. 2016). Mróz et al. (2017) later quantified this population, reporting an occurrence rate of 0.25 such planets per main-sequence star and identifying even shorter events suggestive of Earth- to super-Earth-mass FFPs. The first terrestrial-mass FFP candidate was confirmed by Mróz et al. (2020). Although Gould et al. (2022) estimated that FFPs outnumber bound planets by an order of magnitude, the first quantitative measurement was provided by Sumi et al. (2023). Using nine years of MOA-II data, they constructed the mass function of FFPs down to Earth mass, finding them to be 19^{+23}_{-13} times more abundant than bound planets beyond the snow line, with a total mass of $\sim 171 M_{\oplus}$ per star, suggesting a common formation origin in planetary systems. This abundant population of FFPs has been further supported by the James Webb Space Telescope (JWST) near-infrared survey in the Orion Nebula, which uncovered numerous planetary-mass candidates (Tamura et al. 1998; Oasa et al. 1999; Béjar et al. 1999; Lucas & Roche 2000; Barrado y Navascués et al. 2002; Pearson & McCaughrean 2023).

These observational data suggest that freely floating planets may have been 1) the dominant byproducts of planet formation and 2) major agitators of planetary systems during their dissociation from their host stars. Various formation pathways of FFPs originating from bound planetary systems have been proposed to account for the substantial FFP population observed.

Planet–planet scattering during formation can generate unbound or wide-orbit planetary-mass objects (Zhou & Lin 2007; Ida et al. 2013), while dynamical instabilities in mature, packed systems can excite eccentricities and disrupt planetary architectures (Rasio & Ford 1996; Weidenschilling & Marzari 1996; Lin & Ida 1997; Zhou et al. 2007). The likelihood of ejection increases for lower-mass planets, which require more massive perturbers to be scattered (Veras & Armitage 2005). Additional mechanisms include stellar flybys (Spurzem et al. 2009; Malmberg et al. 2010; Zheng et al. 2015) and post-main-sequence evolution (Adams et al. 2013). For example, circumbinary systems like Kepler-16 and Kepler-34 may eject numerous sub-Neptune-mass planets (Coleman et al. 2023). However, the abundance of ejected Earth-to-Neptune-mass planets remains poorly constrained due to limited studies and uncertainties in the wide-orbit population. Observational studies of solar-type stars reveal that approximately 60% of stars between 0.75 and $1.25 M_{\odot}$ exist in binary systems (Offner et al. 2023). Of these binary systems, about 23% are classified as close binaries (with a separation $(a \leq 3$ au)). Consequently, close binaries are present in roughly 14% of all such stellar systems. This population is significant in the context of planetary ejection. Recent work by Coleman & DeRocco (2025) finds that dynamical interactions with the central binary in close circumbinary systems are likely the dominant progenitor for FFPs more massive than Earth. Conversely, planet–planet scattering in single or wide binary systems dominates the production of lower-mass planets at Mars-mass and below. However, in the study by Guo et al. (2025), which examined FFPs produced by planet–planet scattering in single-star systems, a clear trend emerged: low-mass, close-in planets tend to remain bound to their host stars, while Neptune-like planets on wider orbits dominate the ejected population. This finding is broadly consistent with current observational data.

An alternative origin involves direct gravitational collapse of molecular cloud cores (Luhman 2012), similar to star formation. However, this requires unusually high densities significantly exceeding those in typical star-forming regions to fragment into planetary-mass objects. While this mechanism may contribute, its importance relative to ejection remains uncertain.

In this work, we explore the dynamical consequences of the assumption that most FFPs form near their host stars and are subsequently liberated. We propose that their progenitors likely originate from cold, less-bound orbits, where perturbations from distant massive bodies (e.g., stellar companions or giant planets) excite them onto high-eccentricity paths, a mechanism analogous to high-eccentricity migration invoked for hot Jupiters (Wu & Murray 2003).

Motivated by the prevalence of compact inner systems, we investigate a previously unexplored channel involving strong scattering events between highly eccentric, massive planets and close-in, lower-mass planets. We demonstrate that such interactions can efficiently transfer orbital energy, unbinding the outer planet and producing FFP population.

We briefly recapitulate, in §2.1, various eccentricity excitation mechanisms associated with high-e migration. We derive, in §2.2, the physical basis for this ejection mechanism and determine an analytical criteria for successful ejection. We discuss the role of tidal effects in §2.3 based on an equilibrium-tide prescription in §A. We validate, in §3, this process numerically using high-precision N -body (§3.1) simulations of systems hosting both close-in planets and a cold outer giant. In §4, we examine how tidal dissipation inside the planets and their host stars may modify the dynamics and in §5, we highlight the kinematic changes among the surviving planets. We summarize our findings and discuss their broad implications in §7.

2. RELEVANT PHYSICAL PROCESSES

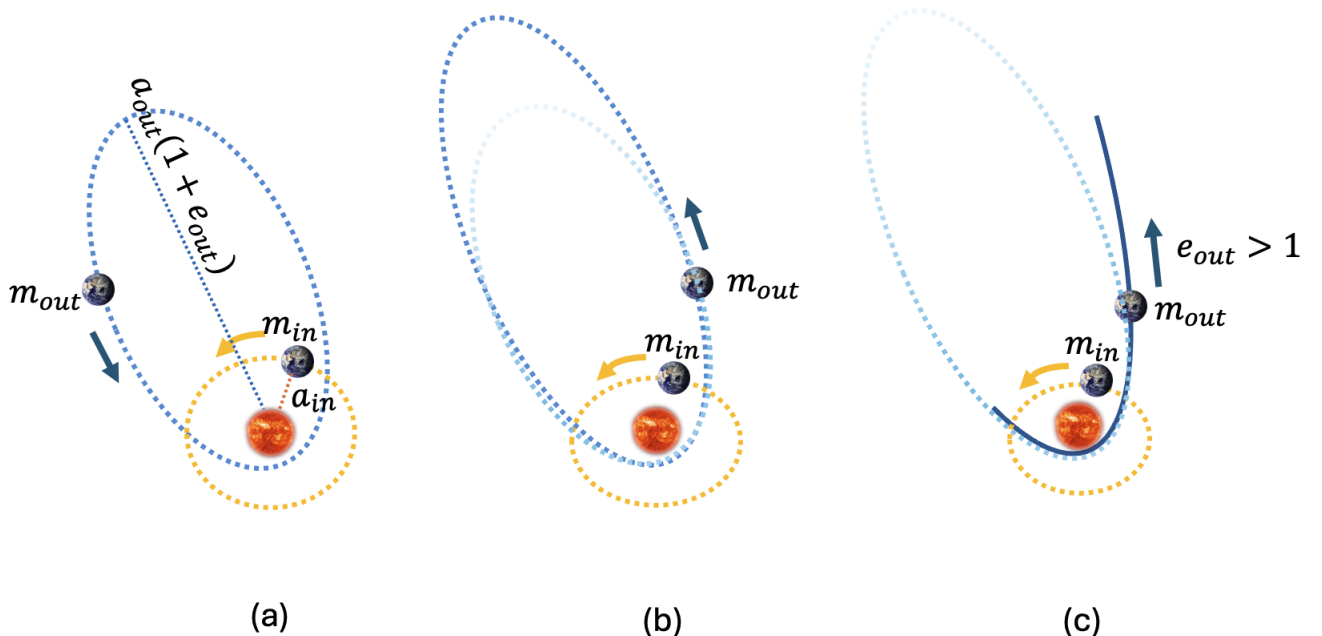


Figure 1. The basic physical mechanism for producing free-floating planets through two-body scattering, depicted across three panels. Panel (a) shows an intruding cold planet (m_{out}), characterized by an extremely eccentric orbit (a_{out} , e_{out}), as it intercepts a short-period super Earth (m_{in}) with a nearly circular orbit (a_{in} , e_{in}). Panel (b) captures the outcome of their close gravitational encounter, where the intruding planet (m_{out}) may gain sufficient energy to transition into a more loosely bound orbit. Panel (c) demonstrates the culmination of this process, where, after several orbital crossings, the intruding planet (m_{out}) undergoes ejection from the system due to the cumulative energy changes from repeated interactions, ultimately becoming a free-floating object.

In Figure 1, we schematically illustrate the physical mechanism for producing free-floating planets (FFPs) via gravitational scattering between close-in planets and cold, eccentric, outer intruders from an outer planetary population. For clarity, the parameters of the close-in planets, including planetary mass (m), semi-major axis (a), eccentricity (e), and inclination (i), are denoted throughout this work as m_{in} , a_{in} , e_{in} and i_{in} , respectively. Analogously, the outer intruders are labeled m_{out} , a_{out} , e_{out} and i_{out} . We consider the systems with $m_{\text{out}} \geq m_{\text{in}}$, $a_{\text{out}} \gg a_{\text{in}}$, and $(1 - e_{\text{out}}^2) \ll 1$ such that $m_{\text{out}}/2a_{\text{out}} < m_{\text{in}}/2a_{\text{in}}$ and $m_{\text{out}}\sqrt{a_{\text{out}}(1 - e_{\text{out}}^2)} < m_{\text{in}}\sqrt{a_{\text{in}}}$.

As depicted in the left panel of Figure 1, an intruding cold planet on a highly eccentric orbit undergoes orbital crossings with the inner planetary population. During successive close encounters, the outer intruder may gain sufficient energy to attain an even more eccentric trajectory (middle panel). Ultimately, it can escape the host star's gravitational influence entirely, as shown in the right panel of Figure 1.

2.1. Excitation of Cold-planets' Nearly Parabolic Orbits

The rich populations of close-in super-Earths and distant cold Jupiters are well-established. We briefly recapitulate two mechanisms that can lead to high-eccentricity excitation for the cold planets and their intrusion to the proximity of their host stars. The underlying mechanism involves secular perturbations induced by a distant perturber. Within the context of this paper, cold perturbers encompass both unseen planets and distant stellar binary companions.

High-resolution observations reveal that complex substructures in protoplanetary disks (PPDs) are ubiquitous around young stars (e.g., van Boekel et al. 2017; Avenhaus et al. 2018; Andrews et al. 2018; Long et al. 2019; Garufi et al. 2020). These features are widely interpreted as signatures of planetary-mass perturbers interacting with their natal disks (Zheng et al. 2017b; Asensio-Torres et al. 2021; Wang et al. 2022). Stellar binaries are also prevalent in the universe. Over half of all star systems host one or more stellar companions, exhibiting diverse orbital configurations.

The ubiquity of such distant companions, including massive planets or long-period stellar-mass companions profoundly influence the architectures of the inner planetary systems. Cold planetary populations, being nearer to these perturbers' gravitational sphere of influence and farther from their host stars, are particularly susceptible. In the following sections (§2.1.1 and §2.1.2), we detail two key mechanisms through which cold companions generate near-parabolic intruders: von Zeipel-Lidov-Kozai (vZLK) oscillation and sweeping secular resonance (SSR). Whereas vZLK is effective, requiring a modest to large inclination between the orbits of the companion and planet, the SSR is a robust mechanism during the final depletion of the planets' natal disk. In §2.1.3, we also assess the dynamical feasibility of systems hosting both a close-in planet and an eccentric outer intruder.

2.1.1. von Zeipel-Lidov-Kozai cycle

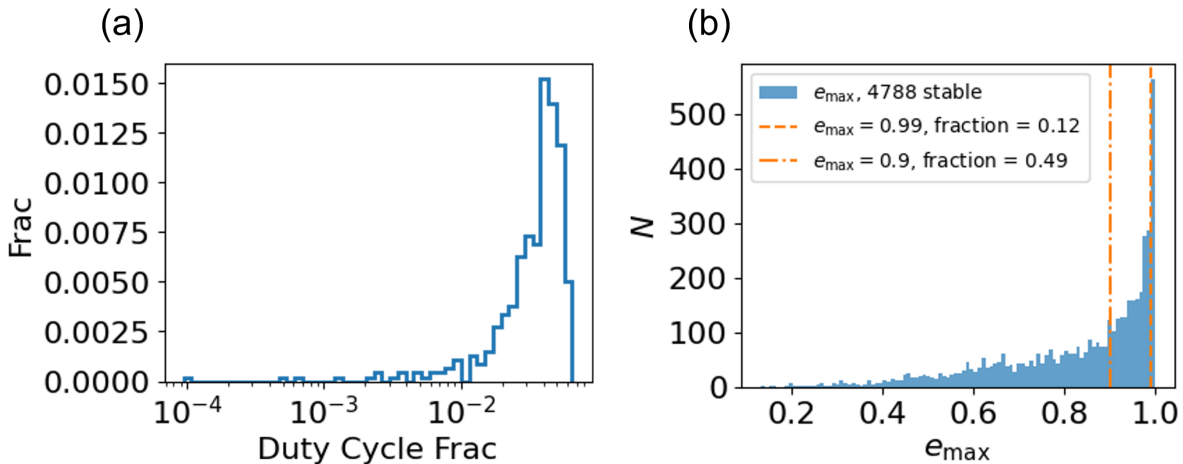


Figure 2. (a) Duty cycle fraction (the cumulative duration of extreme eccentricity excitation ($e > 0.99$) fraction) driven by the von Zeipel-Lidov-Kozai mechanism was quantified in a hierarchical triple system containing a Sun-like primary, a M_\odot stellar companion ($a_{\text{pert}} = 10^3$ au, $e_{\text{pert}} = 0.5$), and a Jupiter-mass planet ($a_{\text{out}} = 10$ au, e_{out} is sampled from a Rayleigh distribution, characterized by the probability density function: $f(e; \sigma) = e/\sigma^2 \exp(-e^2/(2\sigma^2))$, where the scale parameter $\sigma \approx 0.3$). Numerical integrations over 3×10^8 years (neglecting tidal effects) demonstrate repeated eccentricity surges reaching $e_{\text{out}} > 0.99$. (b) Distribution of the theoretical maximum e_{out} attainable by the systems. 12% of the systems can reach $e_{\text{out}} = 0.99$, and 49% can reach $e_{\text{out}} = 0.9$.

The von Zeipel-Lidov-Kozai (vZLK) mechanism, driven by a largely inclined distant perturber induces significant orbital evolution through cumulative angular momentum transport (von Zeipel 1910; Lidov 1962; Kozai 1962; Wu & Murray 2003; Naoz 2016; Bhaskar et al. 2021). This process causes the cold planet to undergo large-amplitude inclination-eccentricity ($i - e$) modulation via resonant coupling. The characteristic vZLK oscillation timescale is

$$\tau_{\text{vZLK}} \simeq (M_\star/M_{\text{pert}})(a_{\text{pert}}/a_{\text{out}})^3(1 - e_{\text{pert}}^2)^{3/2}P_{\text{out}} \gg P_{\text{out}} \quad (1)$$

at $a_{\text{out}} < a_{\text{pert}}$, where a_{out} and P_{out} denote the semi-major axis and orbital period of the cold planet, while $M_{\text{pert}}, a_{\text{pert}}, e_{\text{pert}}$ represent the mass and orbital parameters of the distant perturbing body. For the cold planet in the proximity of

the perturbed, significant eccentricity excitation proceeds efficiently. We present illustrative numerical simulations to demonstrate that eccentricities of cold Jupiters (with $a \gtrsim 10$ au) can be driven to near-parabolic values by a distant perturber (at $\sim 10^3$ au) within a simulation timescale ($\tau_{\text{vZLK}} \sim 10^7$ yr $\leq t_{\text{sim}} \sim 3 \times 10^8$ yr). These models establish this mechanism as a viable pathway for generating highly eccentric orbits for cold planet population.

In order to quantify the cumulative duty cycle of extreme eccentricity excitation ($e > 0.99$) induced by the vZLK mechanism, we conducted numerical simulations using **KozaiPy**, which is an open-source used for hierarchical three-body integration package (<https://github.com/djmunoz/kozaipy>). Our system configuration consists of a Sun-like primary, a solar mass stellar companion with $a_{\text{pert}} = 10^3$ au and $e_{\text{pert}} = 0.5$, and a Jupiter-mass cold planet at $a_{\text{out}} = 10$ au with initial e_{out} chosen from a Rayleigh distribution with $\sigma \approx 0.3$, and a uniform inclination distribution $-1 \leq \cos i \leq 1$.

First, we neglect tidal dissipation within both the planet and the host star. As shown in Figure 2(a), the vZLK-driven high-eccentricity phase occupies approximately 3% of the total simulated time—persisting over 10^6 – 10^7 yr within a 3×10^8 yr integration. This duration substantially exceeds the characteristic ejection timescales of 10^3 – 10^6 yr found for Jupiter-mass systems in our parameter study (see details from the later discussion on the ejection timescale). Such a temporal hierarchy confirms that vZLK-driven extreme eccentricity can indeed serve as a precursor to planetary ejection. We simulated 5000 systems, among which 4788 remained stable. Figure 2(b) indicates that 12% of the systems can reach $e_{\text{out}} = 0.99$, and 49% can attain $e_{\text{out}} = 0.9$. However, if the initial condition is set with $\cos(i)$ uniformly sampled from $[-0.1, 0.1]$, the percentage of systems reaching $e_{\text{out}} = 0.99$ increases to 100%. Therefore, the von Zeipel-Lidov-Kozai (vZLK) effect is one of the potential mechanisms for exciting an intruding planet’s nearly parabolic orbit. This process is due to the secular perturbation induced by a more distant companion planet or star on mutually inclined planes, which leads to periodic modulation in the cold planet’s eccentricity (e_{out}) and inclination (i_{out}).

2.1.2. Sweeping secular resonance

Besides the traditional vZLK mechanism, the sweeping secular resonance (SSR) induced by a depleting gas disk represents a promising alternative pathway for generating highly eccentric planetary orbits (Nagasawa et al. 2000; Nagasawa & Ida 2000; Nagasawa et al. 2003; Nagasawa & Lin 2005; Zheng et al. 2020, 2021). This mechanism operates during the lifetime of the protoplanetary disk through resonant interactions between a cold planet (initially in a low-eccentricity orbit) and a distant perturbing body. The critical physical scenario involves secular resonance, where the precession frequency of the distant perturber matches that induced in the cold planet via the disk’s gravitational potential. At resonance, angular momentum is transferred from the cold planet to the distant perturber without any energy exchanges. This interaction leads to the monotonic excitation of the planet’s eccentricity while its semi-major axis remains unchanged. As the disk depletes, the secular resonance location sweeps inward, traversing an extended radial range. This resonance sweeping process systematically drives eccentricity growth across multiple orbital locations, creating a population of eccentric outer intruders. The asymptotic eccentricity is determined by the sweeping rate of the secular resonance, i.e. the disk depletion timescale. This mechanism shares similarities with secular resonance sweeping effects observed in our solar system dynamics, such as Jupiter’s influence on asteroids’ orbital evolution (Nagasawa et al. 2000; Zheng et al. 2017a).

2.1.3. Secular chaos

Previous studies suggest that highly excited outer planets can facilitate marginally stable orbital configurations for close-in planetary populations (Nagasawa et al. 2008; Nagasawa & Ida 2011). In their numerical simulations, Matsumura et al. (2013) explored the early dynamical evolution of multiple giant planets and their impact on the orbital stability of inner terrestrial worlds. Their results demonstrate that even in scenarios where orbital crossing occurs between an eccentric outer giant and a close-in terrestrial planet, such that the outer giant’s minimum pericenter distance falls within the semi-major axis of the inner planet, a significant fraction of terrestrial worlds still survives within 10 Myr. Notably, this survival rate is enhanced for planets situated close in proximity to their host stars. These findings underscore the resilience of inner planetary orbits under disruptive gravitational perturbations from eccentric, massive companions.

2.2. Energy Exchange during Close Encounters

We consider an outer intruding planet on a nearly parabolic orbit with a semi-major axis $a_{\text{out}} (\gg R_{\star}$, where R_{\star} is the radius of the host star) and an eccentricity $e_{\text{out}} (= 1 - \epsilon$, where $\epsilon \ll 1$). This planet’s total energy and angular

momentum are

$$E_{\text{out}} = -m_{\text{out}} \frac{GM_{\star}}{2a_{\text{out}}} \quad \text{and} \quad h_{\text{out}} = m_{\text{out}} \sqrt{GM_{\star}a_{\text{out}}(1 - e_{\text{out}}^2)}. \quad (2)$$

when its orbit intercepts that of an inner planet with a semi-major axis $\sim a_{\text{in}}$ ($\ll a_{\text{out}}$) and small eccentricity e_{in} . At $\epsilon a_{\text{out}} \ll a_{\text{in}} \ll a_{\text{out}}$, the outer intruder's radial velocity (V_{out}) and kinetic energy (K_{out}) are

$$V_{\text{out}} \simeq (2GM_{\star}/a_{\text{in}})^{1/2} \quad \text{and} \quad K_{\text{out}} \simeq m_{\text{out}}GM_{\star}/a_{\text{in}}. \quad (3)$$

After these two planets undergo a close encounter with an impact parameter b , the impinging planets undergo a change both in velocity (ΔV) and energy (ΔE). With a relative velocity V , the relative momentum perpendicular to the incident relative velocity acquired by the encounter is given with the impulse approximation by a typical gravitational force between the two planets multiplied by a typical passing timescale:

$$\frac{m_{\text{out}}m_{\text{in}}}{(m_{\text{out}} + m_{\text{in}})} \Delta V \sim \frac{Gm_{\text{out}}m_{\text{in}}}{b^2} \frac{2b}{V}. \quad (4)$$

The above impulsive approximation is adequate for close encounters with impact parameters satisfy $(m_{\text{out}} + m_{\text{in}})/V^2 \ll b \lesssim R_{\text{Hill}}$, where $R_{\text{Hill}} = ((m_{\text{in}} + m_{\text{out}})/3M_{\star})^{1/3}a_{\text{in}}$ is planets mutual Hill's radius. Although ΔV is significantly reduced for encounters with $b \gtrsim R_{\text{Hill}}$, the outer intruder continues to cross the inner planet's orbit.

The relative velocity V between the close-in planet and the cold outer intruder for an encounter at $r_{\text{out}} \sim a_{\text{in}}$ is mostly given by a combination of primarily radial velocity V_{out} of the outer planet at $r_{\text{out}} \sim a_{\text{in}}$, and the Keplerian velocity of inner planet, $(GM_{\star}/a_{\text{in}})^{1/2}$, such that $V \sim V_{\text{out}}$. Since

$$\Delta V_{\text{out}} = \frac{m_{\text{in}}\Delta V}{(m_{\text{out}} + m_{\text{in}})}, \quad (5)$$

we obtain in the limit $m_{\text{in}} \ll m_{\text{out}}$,

$$\frac{\Delta V_{\text{out}}}{V_{\text{out}}} \sim \frac{2Gm_{\text{in}}}{bV_{\text{out}}^2}. \quad (6)$$

In this case, while $\Delta V \propto m_{\text{out}}$ (Equation 4), $\Delta V_{\text{out}} \propto \Delta V/m_{\text{out}}$ (Equation 5) so that the m_{out} -dependence drops out in ΔV_{out} in Equation (6). The energy change of the outer planet is $\Delta E \simeq m_{\text{out}}V_{\text{out}}\Delta V_{\text{out}}$ such that

$$\frac{\Delta E}{K_{\text{out}}} \sim \frac{\Delta V_{\text{out}}}{V_{\text{out}}}. \quad (7)$$

Since $K_{\text{out}} \gg |E_{\text{out}}|$, a small fractional change in K_{out} at $r_{\text{out}} \sim a_{\text{in}}$ can result in ejection of the outer planet. Moreover, $\Delta E/K_{\text{out}}$ is independent of m_{out} and ΔE is also independent of a_{in} .

Combining these equations, we find

$$\left| \frac{\Delta E}{E_{\text{out}}} \right| \simeq \frac{m_{\text{in}}a_{\text{out}}}{M_{\star}b} = 0.07 \frac{m_{\text{in}}}{M_{\oplus}} \frac{M_{\odot}}{M_{\star}} \frac{a_{\text{out}}}{1 \text{ au}} \frac{R_{\oplus}}{b}. \quad (8)$$

The above equation implies an encounter-ejection criteria, $\Delta E/E_{\text{out}} \gtrsim 1$ with

$$\frac{b}{R_{\oplus}} \lesssim 0.07 \frac{m_{\text{in}}}{M_{\oplus}} \frac{M_{\odot}}{M_{\star}} \frac{a_{\text{out}}}{1 \text{ au}}. \quad (9)$$

Encounters with smaller impact parameters would lead to $\Delta E \gtrsim E_{\text{out}}$ and hyperbolic encounters, albeit they occur less frequently (see below). The independence of $|\Delta E/E_{\text{out}}|$ and b/R_{\oplus} of a_{in} arises only for planet pairs with crossing orbits.

Around G and M dwarf stars (with $M_{\star} \lesssim 1M_{\odot}$), collision-free (dissipationless) encounters between a super-Earth with $m_{\text{in}} \simeq 10M_{\oplus}$ (regardless of a_{in}) and an outer intruder with $m_{\text{out}} \gtrsim 10M_{\oplus}$ at $a_{\text{out}} \gtrsim 10\text{au}$ can lead to $|\Delta E/E_{\text{out}}| \gtrsim 1$ (Equation 8), with either positive or negative sign, provided the sum of their radii R_{out} and R_{in} is less than $7R_{\oplus}$. Such large fractional energy change introduces the ejection probability for the intruding planet. Note that these conditions are independent of m_{out} . Close encounters without physical collision can also lead to the ejection of Jupiter-mass gas giants on more extended orbits ($a_{\text{out}} \gtrsim 20 \text{ au}$) by a super-Earth with a $m_{\text{in}} \gtrsim 10M_{\oplus}$ provided $R_{\text{out}} + R_{\text{in}}$ does not exceed $14 R_{\oplus}$.

These conditions are also independent of a_{in} where the the planets' orbits cross each other. But their occurrence frequency is

$$\omega_c \simeq (b/a_{\text{in}})^2 \Omega_{\text{out}} \quad \text{where} \quad \Omega_{\text{out}} = (GM_{\star}/a_{\text{out}}^3)^{1/2}. \quad (10)$$

If these planets' orbits persistently cross each other, the corresponding occurrence timescale is

$$\tau_c \simeq \frac{1}{\omega_c} \simeq \frac{R_{\oplus}^2}{b^2} \frac{a_{\text{in}}^2}{R_{\odot}^2} \frac{a_{\text{out}}^{3/2}}{\text{au}^{3/2}} 10^4 \text{yr} \simeq 2 \frac{M_{\oplus}^2}{m_{\text{in}}^2} \frac{M_{\star}^2}{M_{\odot}^2} \frac{\text{au}^{1/2}}{a_{\text{out}}^{1/2}} \frac{a_{\text{in}}^2}{R_{\odot}^2} \text{Myr}. \quad (11)$$

This associated chaotic lifetime is set by the combined rates of ejection and merger events. For encounters between a nearly parabolic cold planet (with $a_{\text{out}} \lesssim 10^2$ au) and a typical super-Earth (with $m_{\text{in}} \gtrsim 10M_{\oplus}$ and $a_{\text{in}} \lesssim 0.1$ au), τ_c is generally much shorter than the multi-Gyr lifespan of G and M dwarfs. If during a fraction (f) of the vZLK cycle the outer planet's peri-center distance $a_{\text{out}}(1 - e_{\text{out}}) < a_{\text{in}}$, the occurrence timescale for an ejection or a merger event would be lengthened to $\tau'_c = \tau_c/f$.

2.3. Tidal Dissipation

Tidal dissipation also leads to planet's eccentricity evolution (Fabrycky & Tremaine 2007; Nagasawa et al. 2008; Nagasawa & Ida 2011). In principle, the tidal torque is a vector which depends on the spin vectors of the planet (Ω_p) and its star's (Ω_{\star}) as well its orbital angular momentum vector (\mathbf{A}_p) (Eggleton et al. 1998). It leads to changes in the planet's Runge-Lenz vector $\dot{\mathbf{e}}$ (Murray & Dermott 1999). For simplicity, we consider the limiting case that all of these vectors are aligned.

In the equation of motion for individual planets, contribution due to the equilibrium-tidal dissipation can be incorporated into the total force (Hut 1981)

$$\mathbf{F} = -G \frac{Mm}{r^2} \left\{ \mathbf{e}_r + 3q \left(\frac{R}{r} \right)^5 k_2 \left[(1 + 3\frac{\dot{r}}{r}\tau_{\text{lag}}) \mathbf{e}_r - (\Omega - \dot{\theta})\tau_{\text{lag}} \mathbf{e}_{\theta} \right] \right\}, \quad (12)$$

where M and m represent the masses of the tidally deformed body and the perturbing companion (they can be either the intruding planet and its host star or the other way around) respectively; $q = m/M$; r is the separation distance between their centers of mass respectively; R corresponds to the radius of the tidally affected body; k_2 is the perturbed body's tidal Love number; τ_{lag} signifies a constant small time lag accounting for tidal amplitude and directional lag (§4); Ω and $\dot{\theta}$ denote the rotational angular velocity of the deformed body and the orbital angular velocity of the companion (true anomaly rate), respectively; while \mathbf{e}_r and \mathbf{e}_{θ} are radial and tangential unit vectors in polar coordinates. The conventional quality factor is $Q = 1/\omega_{\text{tide}}\tau_{\text{lag}}$ where $\omega_{\text{tide}} = \Omega - \dot{\theta}$ is the tidal forcing frequency.

For the numerical simulations in §3, we adopt \mathbf{F} in Equation (12) for both the host star and the planets. For illustration purpose, we briefly adopt, here, some simplifying approximations to highlight the main effects of the star's tidal torque on the orbit of the intruding planet. Since the interaction between a star and its planet is symmetric, we can first consider only the case where the planet remains rigid. For deformable bodies such as gas giants, the calculations can be applied inversely, and the effects from both scenarios summed together. So changes in the star-planet's orbital angular momentum is caused by the combined tidal torque of the deformed planet (or star) on the star (or planet)

$$\mathbf{\Gamma}_{\text{tot}} = \mathbf{\Gamma}_{\star} + \mathbf{\Gamma}_p, \quad \text{where} \quad (13)$$

$$\mathbf{\Gamma}_{\star,p} = \mathbf{r} \times \mathbf{F}_{\star,p} = 3G \frac{M_{\star,p}}{r} \left(\frac{R_{p,\star}}{r} \right)^5 k_2^{p,\star} \left[(\Omega_{p,\star} - \dot{\theta}_{p,\star})\tau_{\text{lag}}^{p,\star} \mathbf{e}_z \right], \quad (14)$$

respectively, with $M = M_{p,\star}$, $m = M_{\star,p}$, $q = M_{\star,p}/M_{p,\star}$, and $R = R_{p,\star}$ in Eq. 12. For the discussion on tidal interaction, M_p and M_{\star} refers to the mass of the planet and its host star. Similarly, $k_2^{p,\star}$ and $\tau_{\text{lag}}^{p,\star}$ refer to the Love number and lag time of the planet and star, respectively.

For a nearly parabolic orbit, tidal interaction occurs predominantly during peri-center passage with $\Delta T \sim 2\pi/\dot{\theta}(r_{\text{peri}}) \sim \epsilon^{3/2}P$ where $\epsilon = 1 - e$, $r_{\text{peri}} = \epsilon a$ is the perigee distance, $P = 2\pi/\Omega_{\text{out}}$ and a are the period and semi-major axis respectively. Eccentricity damping is mostly induced by tidal dissipation in the planet during its peri-center passage. Averaged over many orbits (§A), the eccentricity (as well as a and P) evolves on a timescale

$$\tau_e = e/\dot{e} \propto \mathcal{O}(\epsilon P/q^{2/3}k\tilde{\tau}_n\tilde{R}^5) \quad (15)$$

where $k = k_2^p$, the normalized $\tilde{\tau}_n = \tau_{\text{lag}}^p / \Delta T$ and $\tilde{R} = R_p / R_R$ with $R_R = q^{1/3}(1 - e)a_p$ is the Roche radius at perigee (Eq. A27). Adopting $R_p = R_J$, $r_{\text{peri}} = 0.1$ au, $M_p = M_J$, $M_\star = 1M_\odot$, $e_p = 0.99$, $a_p = 10$ au (Table 1), we find $P \simeq 30$ yr, $r_{\text{peri}} = 0.1$ au, $\tilde{R} \simeq 0.05$, $\Delta T \simeq 10^6$ s, with $g_{12} \simeq 20.08$, $g_{22} \simeq 88.85$, $g_{32} \simeq 307.01$, and $g_{42} \simeq 26.87$ in Eqs. (A12) and (A23). We take Jupiter's $\Omega = 2\pi/(10 \text{ hr}) = 1.7 \times 10^{-4} \text{ s}^{-1}$, $k \simeq 0.3$, and $\tau_{\text{lag}}^p \simeq 10^{-7} \text{ yr}$ (§4), we infer from Eq. 15, $\tilde{\tau}_n \simeq 3.2 \times 10^{-6}$, $\tilde{\tau}_\Omega \simeq 8.9 \times 10^{-5}$. Applying these estimates to Eq. (A27), we find $\tau_e \gtrsim 10^8$ yr.

In our settings, the characteristic vZLK oscillation timescale $\tau_{\text{vZLK}} \simeq 2 \times 10^7$ yr (Eq. 1). The results in Fig. 2 show that typical duty cycle for a planet to attain $r_{\text{peri}} \lesssim 0.1$ au is $\sim 0.03\tau_{\text{vZLK}} \sim 6 \times 10^5$ yr. Since this time scale is much smaller than τ_e , we do not anticipate the tidal damping of eccentricity to significantly modify the outer planet's probability of acquiring sufficiently high e_{out} , through the vZLK effect, to cross the orbit of the inner planet. But in the limit $e_{\text{out}} \gtrsim 0.999$, r_{peri} is a factor of two larger than the stellar radius R_\star . As $\tilde{R} \rightarrow 1$ and $\tilde{\tau}_n$ increases, τ_e becomes $\lesssim \tau_{\text{vZLK}}$. Tidal dissipation enhances orbital decay, inflation, and planet-star merger rate. These assessments are in agreement with the results of numerical simulations in §4.

3. NUMERICAL SIMULATIONS

3.1. Computational Method and Model Parameters

To explore the orbital dynamics of eccentric outer planets influenced by close encounters with the inner planetary population, we employ the open-source N -body code **REBOUND** (Rein & Liu 2011), enhanced with the **REBOUNDx** library (Tamayo et al. 2020). This extension allows incorporation of complex additional forces into simulations, including velocity-dependent effects such as tidal interactions or relativistic corrections.

For numerical integration, we utilize the IAS15 algorithm, a 15th-order, adaptive-timestep integrator (Everhart 1985; Rein & Spiegel 2015). As a non-symplectic method, IAS15 is designed for high-precision simulations involving close encounters or arbitrary forces. Its adaptive stepping mechanism dynamically adjusts the integration step size based on error estimates, ensuring accuracy during planetary close approaches. This robustness makes IAS15 particularly well-suited for studying orbital evolution in systems with dynamically unstable or hierarchical configurations. And all bodies have a finite size and merge directly if there are physical collisions (the distance between two particles is closer than the sum of their radii). Furthermore, the planets with positive orbital energy ($E > 0$) and located at large distances ($r > 1000$ au) from their host star are assumed to have undergone gravitational ejection from their original system. For all the simulations presented in this paper, we run simulations up to 10 Myr, unless stated otherwise.

To investigate the feasibility of inducing a nearly parabolic trajectory through gravitational interactions, we model a three-body dynamical system comprising a solar-like host star ($M_\star = M_\odot$, $R_\star = R_\odot$) and two planets. The intruding planet (also a designated outer planet) is initialized with a semi-major axis (a_{out}) of either 10 au or 20 au and an eccentricity (e_{out}) of 0.999 or 0.99 or even 0.9, mimicking highly elongated initial conditions. We consider three archetypal planet types for the outer planet: a super-Earth planet with $m_{\text{out}} = 10M_\oplus$ and $R_{\text{out}} = R_\oplus(m_{\text{out}}/M_\oplus)^{1/3}$ or a Jupiter-mass giant planet with $m_{\text{out}} = M_J$ and $R_{\text{out}} = R_J$ or a Earth-like planet with $m_{\text{out}} = M_\oplus$ and $R_{\text{out}} = R_\oplus$. The close-in planet (also designated inner planet) is assumed to have a circular orbit ($e_{\text{in}} = 0$) initially throughout the work. The mass and semi-major axis of the close-in planets vary across a broad range. Taking the density divergence between rocky-like super-Earth and gaseous giant into consideration, the physical radii of the close-in planet are modeled using a piecewise function:

$$R_{\text{in}} = \begin{cases} R_\oplus(m_{\text{in}}/M_\oplus)^{1/3} & m_{\text{in}} \leq 10M_\oplus, \\ R_\oplus(10)^{1/3} + R_J[(m_{\text{in}} - 10M_\oplus)/M_J]^{1/3} & 10M_\oplus < m_{\text{in}} < M_J, \\ R_J & m_{\text{in}} = M_J. \end{cases} \quad (16)$$

These settings ensure a smooth physical size transition between the Jupiter-like gas giant and super-Earth planets. For a more general stellar mass M_\star , the radius of solar-type stars $R_\star \simeq R_\odot(M_\star/M_\odot)^{0.6}$ where R_\odot is the solar radius.

3.2. Planetary ejection and retention

Figure 3 highlights distinct dynamical behaviors of three representative successful-ejection events, including orbital instability and close encounters, as evidenced by abrupt changes in semi-major axes and eccentricity variations. In all cases, the outer intruder planet is initially set with a semi-major axis of 20 au and a Jovian mass. The results indicate that a massive Jupiter-mass close-in planet is more likely to eject outer intruders effectively.

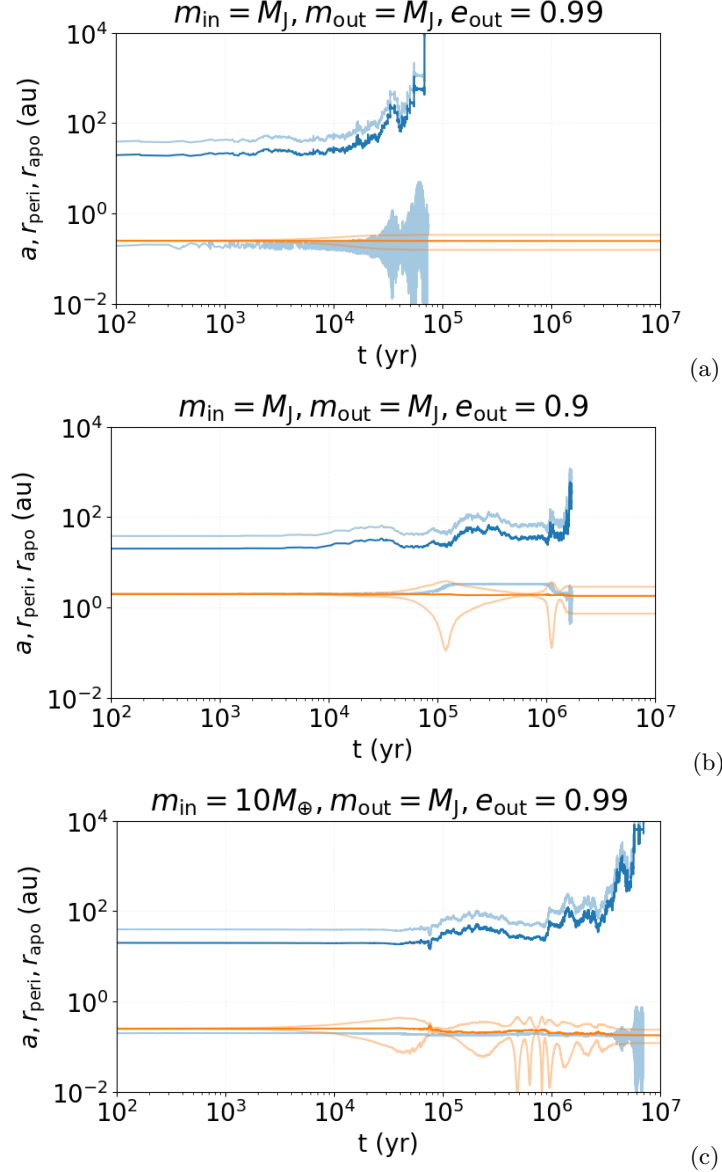


Figure 3. Evolution of the orbital elements $r_{\text{peri}} = a(1 - e)$, a , and $r_{\text{apo}} = a(1 + e)$ for a representative two-planet system over 10^7 years. The outer planet is represented by blue lines (dark line: semi-major axes a ; light lines: pericenter q and apocenter Q), while the close-in planet is shown in orange. Parameters in (a) are $m_{\text{in}} = m_{\text{out}} = M_J$, $R_{\text{out}} = R_{\text{in}} = R_J$, $e_{\text{out}} = 0.99$, $e_{\text{in}} = 0$, $a_{\text{out}} = 20$ au, $a_{\text{in}} = 0.25$ au. Parameters in (b) are $m_{\text{in}} = m_{\text{out}} = M_J$, $R_{\text{out}} = R_{\text{in}} = R_J$, $e_{\text{out}} = 0.9$, $e_{\text{in}} = 0.99$, $a_{\text{out}} = 20$ au, $a_{\text{in}} = 2$ au. Parameters in (c) are $m_{\text{in}} = 10M_{\oplus}$, $R_{\text{in}} = R_{\oplus}(m_{\text{in}}/M_{\oplus})^{1/3}$, $m_{\text{out}} = M_J$, $R_{\text{out}} = R_J$, $e_{\text{out}} = 0.99$, $e_{\text{in}} = 0.99$, $a_{\text{out}} = 20$ au, $a_{\text{in}} = 0.25$ au.

However, this ejection mechanism exhibits inherent randomness, as the outer intruder does not monotonically gain energy during each close encounter with the close-in planet. This stochastic nature is reflected in the orbital evolution of the outer planet, where its semi-major axis is temporarily chaotic after some weak scattering events, and ejection only occurs following a threshold number of encounters.

According to the corresponding occurrence timescale for the ejection event as estimated in Equation (11), the outer intruder can be ejected by a Jupiter-mass inner planet (with $a_{\text{in}} = 0.25$ au) within $\sim 10^5$ yrs. If the outer intruder is less eccentric with an initial eccentricity $e_{\text{out}} = 0.9$, in order to have a close encounter with such an outer intruder, the close-in planet must be positioned at the pericenter distance (to the host star) of the outer planet as $a_{\text{in}} = a_{\text{out}}(1 - e_{\text{out}}) = 2$ au, the estimated ejection timescale increases to $\sim 10^6$ yrs. Most interestingly, even a super-Earth inner planet (with $m_{\text{in}} = 10M_{\oplus}$) is capable of kicking a Jovian planet out of the system within 10 Myr.

This inference may potentially account for the large number of unbounded Jovian mass free-floating planets predicted based on the observed distribution of Einstein radius crossing timescale (Sumi et al. 2011).

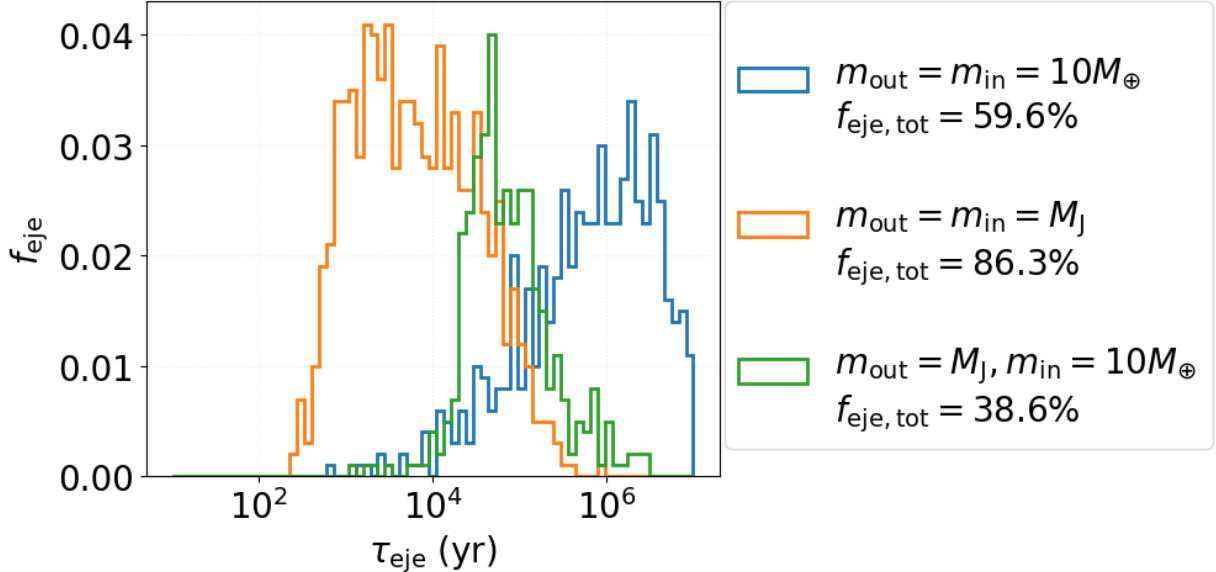


Figure 4. The distribution of ejection timescale (τ_{eje}) of the outer planet. The fiducial settings are: $a_{\text{out}} = 10$ au, $e_{\text{out}} = 0.99$, $a_{\text{in}} = 0.1$ au, $e_{\text{in}} = 0$. The ejection fraction is defined as $f_{\text{eje}} = dN_{\text{eje}}/d\log_{10}(\tau_{\text{eje}}/\text{yr})/N_{\text{tot}}$, where $N_{\text{tot}} = 1000$ is the total number of simulated systems (identical for all three cases). The masses of the close-in planet and the outer planet are compared with various cases. We simply test three mass configurations: $m_{\text{out}} = m_{\text{in}} = 10M_{\oplus}$ (blue steps), $m_{\text{out}} = m_{\text{in}} = M_{\text{J}}$ (orange steps), and $m_{\text{out}} = M_{\text{J}}, m_{\text{in}} = 10M_{\oplus}$ (green steps).

3.3. Ejection timescale

In Figure 4, we present a statistical analysis of the ejection timescales for three distinct mass ratios between the intruding planet and the close-in planet, aiming to investigate the dependence on mass parameters. The blue steps correspond to the case where $m_{\text{out}} = m_{\text{in}} = 10M_{\oplus}$, the orange steps represent $m_{\text{out}} = m_{\text{in}} = M_{\text{J}}$, and the green steps indicate a scenario where the outer intruder planet is significantly more massive than the close-in planet, specifically $m_{\text{in}} = 10M_{\oplus}$ and $m_{\text{out}} = M_{\text{J}}$. The orbital parameters for the outer planet are configured with an extremely eccentric orbit ($e_{\text{out}} = 0.99$) and a semi-major axis of 10 au, while the inner planet is positioned at 0.1 au to facilitate orbital crossing with the outer planet. Each model configuration is simulated across 1000 systems to ensure statistical robustness.

Our analysis reveals that the ejection timescale of the intruding planet exhibits minimal dependence on its mass, aligning well with the analytical estimation (Eq. 11) that collisional conditions are independent of m_{out} . However, the total ejection frequency demonstrates a clear correlation with the outer intruder's mass, as a more massive outer intruder is naturally more resistant to being ejected from the system. Consequently, the ejection frequency within 10 Myr is $\sim 60\%$ for the $m_{\text{out}} = m_{\text{in}} = 10M_{\oplus}$ case and $\sim 39\%$ in the $m_{\text{out}} = M_{\text{J}}, m_{\text{in}} = 10M_{\oplus}$ model. In the context of intuitive planetary dynamics, a high-mass, close-in Jupiter exhibits a remarkable capacity to efficiently eject Jupiter-mass intruders from the outer system. This is exemplified by the case where both planets are Jupiter-mass ($m_{\text{out}} = m_{\text{in}} = M_{\text{J}}$), which yields a robust ejection frequency of nearly $\sim 86\%$ within 10 Myr. These systems also exhibit short ejection timescales, with a significant fraction of outer planets removed within 0.01 Myr. This rapid timescale aligns with the estimation $\tau_{\text{eje}} \propto 1/m_{\text{in}}^2$ from Equation 11. Consequently, a Jupiter-mass inner planet leads to prompt ejections (orange step), whereas a super-Earth requires a much longer time to eject a Jupiter-mass outer planet (blue step).

This trend is further emphasized by the unstable timescale estimated in Equation (11), which predicts that an Earth-mass inner planet would require several million years to eject the outer planet. These findings collectively underscore the critical role of the inner planet's mass in determining both the frequency and timescale of planetary ejections.

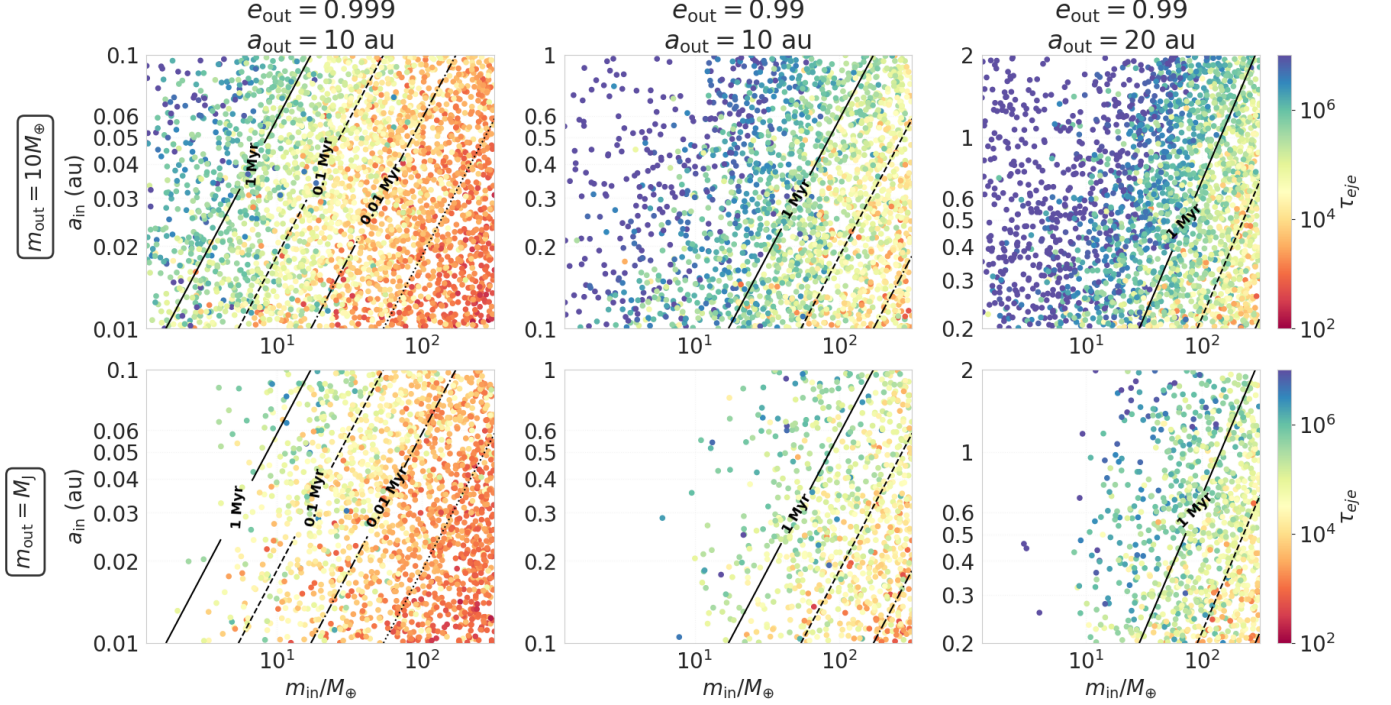


Figure 5. The figure illustrates how the escape timescale of the outer planet varies with the mass (m_{in}) and initial semi-major axis (a_{in}) of the inner planet. Both quantities are generated with a uniform logarithmic distribution. In the top panels, the outer planet is assigned a fixed mass of 10 Earth masses ($10M_{\oplus}$), whereas in the bottom panels, it assumes a Jupiter mass (M_J). Across the three panels, distinct orbital parameters of the outer planet are employed. Left panels: $a_{\text{out}} = 10$ au, $e_{\text{out}} = 0.999$; Middle panels: $a_{\text{out}} = 10$ au, $e_{\text{out}} = 0.99$; Right panels: $a_{\text{out}} = 20$ au, $e_{\text{out}} = 0.99$. The color bar indicates the escape timescale of the outer planet. Additionally, contours of the escaping occurrence timescale, based on Equation (11), are plotted for comparison.

In Section 2.2 we derived the encounter–ejection criterion presented in Equation (9). It reveals that an outer planet can be ejected regardless of its own mass, m_{out} , and irrespective of the inner planet’s semi-major axis, a_{in} . By contrast, the timescale on which instability manifests, whether through mergers or ejections, sensitive with a_{in} (Equation 11). Both the instability threshold and its associated timescale do, however, depend on the outer planet’s semi-major axis, a_{out} . This dependence is physically intuitive, the wider the orbit, the smaller the binding energy, and the more readily the planet is dislodged.

3.4. Stellar collision and planetary merger

The results in Figure 4 also indicate a substantial fraction of the system avoided ejection. Most of these cases are associated with collisional mergers of the inner planets with their host stars (Fig. 6). Angular momentum transfer from the inner to the outer planets during the close encounters leads to the excitation of e_{in} with a fractional change in a_{in} . We assume planets are consumed by their host stars when their $r_{\text{peri}} \leq R_{\star}$. In principle, the inner and outer planets can also merge when their impact parameter is less than the sum of their radii. Only a smaller fraction involve planet–planet collisions, with merger frequencies of 3.3%, 1.1% and 3.7% for $m_{\text{in}} = m_{\text{out}} = 10M_{\oplus}$, $m_{\text{in}} = m_{\text{out}} = M_J$ and $m_{\text{in}} = 10M_{\oplus}, m_{\text{out}} = M_J$ configurations, respectively. This difference is due to planet–planet mergers requiring smaller impact parameters than that for small-angle deflections which lead to planet–star collision courses. In the very small remaining fraction of ejection-free systems, close encounters between the planets can lead to significant eccentricity excitation of the inner planet and changes in the semi-major axis of the outer planets. Further discussions of these outcomes are presented in §5.

3.5. Ejection probability

To validate the robustness of our analytical framework, we conducted extensive numerical simulations to determine the ejection probability and time scale across a broad range of a_{in} and m_{in} values for a fixed outer planet configuration

in Figure 5. Specifically, we examined two distinct scenarios: one where the outer planet is a classical super-Earth with a mass of 10 Earth masses (illustrated in the top panels of Figure 5), and another where the outer planet is a Jupiter-mass planet (depicted in the bottom panels of Figure 5).

To model a more physically representative ejection scenario, we identify cold planets that remain marginally bound to the system at the simulation endpoint (10 Myr) but exhibit severely weakened gravitational binding. These systems satisfy $a_{\text{out},t=10 \text{ Myr}} \gg a_{\text{out},t=0}$ and $e_{\text{out},t=10 \text{ Myr}} > e_{\text{out},t=0}$, indicating extreme orbital expansion and eccentricity growth. Given their dynamical state, such planets are highly susceptible to eventual ejection. For classification simplicity, we assign all such cases an ejection timescale of $\tau_{\text{eje}} = 100 \text{ Myr}$.

Three distinct sets of orbital elements were employed to characterize the outer planet: $a_{\text{out}} = 10 \text{ au}$ with $e_{\text{out}} = 0.999$, $a_{\text{out}} = 10 \text{ au}$ with $e_{\text{out}} = 0.99$, and $a_{\text{out}} = 20 \text{ au}$ with $e_{\text{out}} = 0.99$. These correspond to the left, middle, and right panels of Figure 5, respectively. The close-in planet was assigned masses (m_{in}) with a uniform logarithmic distribution, masses ranging from M_{\oplus} to M_J . The semi-major axis of the inner planet's a_{in} was determined based on the perigee of the outer planet to ensure close encounters between the two planets during simulations. Consequently, for the outer planet with $a_{\text{out}} = 10 \text{ au}$ and $e_{\text{out}} = 0.999$, the inner planet's a_{in} was specified with a uniform logarithmic distribution between 0.01 au and 0.1 au. For the outer planet with $a_{\text{out}} = 10 \text{ au}$ and $e_{\text{out}} = 0.99$, the close-in planet's a_{in} was distributed between 0.1 au and 1 au. Finally, for the outer planet with $a_{\text{out}} = 20 \text{ au}$ and $e_{\text{out}} = 0.99$, the close-in planet's a_{in} was distributed between 0.2 au and 2 au.

Figure 5 represents a statistical analysis of the ejection timescale of the outer planet as a function of a_{in} and m_{in} . The color bar indicates the ejection timescale derived from our simulations. Additionally, analytical estimations of the instability timescale (Equation 11) are overlaid as contour plots. The contours representing 1 Myr, 0.1 Myr, 0.01 Myr, and 1000 yr are depicted with solid, dashed, dash-dotted, and dotted lines, respectively. Each model comprises 4000 simulations.

As discussed in Section 2.2, for a fixed outer planet, the inner planet can efficiently eject the intruder on a shorter timescale when it possesses a larger mass and a smaller semi-major axis ($\tau_c \propto a_{\text{in}}^2/m_{\text{in}}^2$). However, the minimum semi-major axis of an inner planet must satisfy the condition $a_{\text{in}} \geq a_{\text{out}}(1 - e_{\text{out}})$. Notably, a close-in gas giant planet can eject an extremely eccentric outer planet within 0.01 Myr, regardless of whether the outer intruder is a super-Earth or a Jupiter-mass gas giant. For warm super-Earths (with $m_{\text{in}} \sim \text{few } M_{\oplus}$ and $a_{\text{in}} \sim 1 \text{ au}$), it is still feasible to eject either a super-Earth or even a Jupiter from the system, albeit on a timescale extended to several Myr.

In §2.2, we demonstrated that the encounter-ejection criterion is independent of m_{out} and a_{in} , though the instability timescale depends on a_{in} . However, Figure 5 exhibits an apparent degeneracy with this conclusion, as the ejection fraction varies with both a_{in} and m_{out} . Our analytic encounter-ejection criterion (§2.2) requires close encounters with sufficiently small impact parameters for significant energy exchange. These encounters include mergers (occurring when the impact parameter is smaller than the sum of the planet+star or planet+planet radii), which compete with the ejection events. To resolve this discrepancy, we plot the combined fractions of ejections and mergers in Figure 6. This quantity reveals that the total unstable fraction (mergers + ejections, red steps) is largely independent of a_{in} and m_{out} , remaining near $\sim 6\%$ across all models. The observed independence of the total unstable fraction from a_{in} and m_{out} aligns with Equation (9), confirming that while the branching ratio (merger vs. ejection) depends on parameters, the onset of instability does not.

The lower panels of Figure 5 (for $m_{\text{out}} = M_J$) show a scarcity of ejection for systems with relatively small m_{in} . This can be understood from energy conservation. The total (binding) energy of the system is $E = -GM_{\star}(m_{\text{in}}/2a_{\text{in}}) - (m_{\text{out}}/2a_{\text{out}})$, and to eject the outer planet, the semi-major axis of the inner planet must shrink to a value satisfying

$$\frac{a'_{\text{in}}}{a_{\text{in}}} \leq \frac{m_{\text{in}}a_{\text{out}}}{(m_{\text{in}}a_{\text{out}} + m_{\text{out}}a_{\text{in}})}. \quad (17)$$

This energy constraint leads to markedly different outcomes for different planetary masses. In systems with a lower-mass outer planet ($m_{\text{out}} = 10M_{\oplus}$ at $a_{\text{out}} = 10 \text{ au}$), ejecting the outer planet requires only a minor reduction in a_{in} . Furthermore, the ejection condition (Eq. 9) can be satisfied with a relatively large impact parameter ($b \geq R_{\text{in}} + R_{\text{out}}$). As a result, the integrated ejection probability exceeds the merger probability (upper panel of Fig. 6). This ejection probability is even higher for outer planets at $a_{\text{out}} = 20 \text{ au}$, as they are less tightly bound.

In contrast, ejecting a Jupiter-mass planet ($m_{\text{out}} = M_J$) requires a much more significant energy exchange. For inner planets with $m_{\text{in}} \lesssim 3M_{\oplus}$ and initial $a_{\text{in}} \lesssim 0.1 \text{ au}$, Equation (17) implies that a'_{in} must decrease so drastically that the inner planet's pericenter distance falls below either the stellar radius R_{\star} or the tidal disruption distance d_{TDE} (Eq.

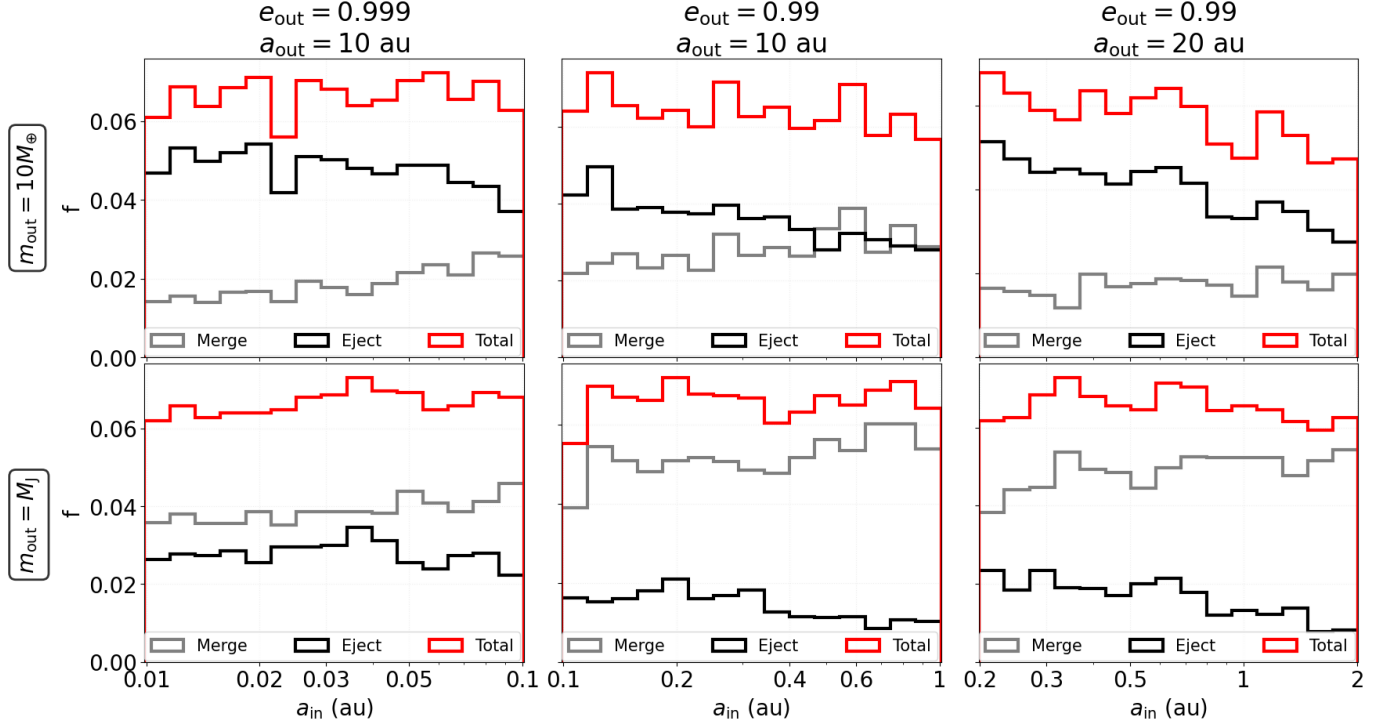


Figure 6. Fraction of planetary systems experiencing mergers or ejections. These quantities are integrated over a_{in} 's uniform logarithmic distribution shown in Fig. 5. The evolution of systems with an outer intruder planet is shown as a function of the initial close-in planet semi-major axis (a_{in}). The black step function shows the fraction of systems where the intruder planet was ejected. The grey step function shows the fraction where planets merged (mostly) with their host stars. The red step function shows the total unstable fraction (mergers + ejections). Top row: Outer intruder mass = $10M_{\oplus}$. Bottom row: Outer intruder mass = M_{J} . Columns (left to right): $a_{\text{out}} = 10$ au, $e_{\text{out}} = 0.999$; $a_{\text{out}} = 10$ au, $e_{\text{out}} = 0.99$; $a_{\text{out}} = 20$ au, $e_{\text{out}} = 0.99$.

18). Consequently, for these systems, it is marginally more likely for the inner planet to be eliminated through a stellar merger than for the Jupiter-mass planet to be ejected as an FFP. This is consistent with the encounter-ejection criteria (Eq. 9), which for these compact systems requires a small impact parameter ($b \lesssim R_{\text{in}} + R_{\text{out}}$), making a merger more probable than an ejection (§2.2). The same trend is reflected in the Safronov-number perspective (Safronov 1972). The gravitational focusing factor for the inner planet, $\Theta = v_{\text{esc}}^2/v_{\text{Kep}}^2 = 2(m_{\text{in}}/M_{\star})(a_{\text{in}}/R_{\text{in}}) \ll 1$, is very small for low-mass ($\lesssim 3M_{\oplus}$), close-in planets. Such a low Θ indicates that physical mergers dominate over pure gravitational scattering, consistent with the outcome that stellar ingestion is more probable than the ejection of a Jupiter-mass companion.

4. LIMITED TIDAL INFLUENCE

To assess the influence of tidal effects on dynamical ejections, we conducted numerical simulations using the REBOUNDx framework (Tamayo et al. 2020) and its constant time lag tidal model (Baronett et al. 2022). We initialized a two-gas-giant and a two-super-Earth systems, around a Solar-mass star. The inner and outer planets had semi-major axes of $a_{\text{in}} = 0.1$ au and $a_{\text{out}} = 10$ au, respectively. The inner planet began on a circular orbit ($e_{\text{in}} = 0$), while the outer planet was placed on a highly eccentric orbit ($e_{\text{out}} = 0.99$). The outer planet's orbital orientation was randomized: its inclination followed an isotropic distribution ($\cos i_{\text{out}} \sim \mathcal{U}[-1, 1]$), and its argument of periastron (ω_{out}), longitude of the ascending node (Ω_{out}), and true anomaly (f_{out}) were drawn uniformly from $\mathcal{U}[0^\circ, 360^\circ]$.

For tidal dissipation, we used a stellar Love number of $k_2^* = 0.035$ and a planetary Love number of $k_2^p = 0.3$ (Ogilvie 2014). The constant time lag for the star was fixed at $\tau_{\star} = 10^{-5}$ yr. We tested three planetary time lags ($\tau_p = 10^{-5}, 10^{-7}, 10^{-8}$ yr) and found the ejection timescale to be largely insensitive to this parameter. Consequently, we adopted an intermediate value of $\tau_p = 10^{-7}$ yr for all subsequent simulations for Jupiter and $\tau_p = 10^{-5}$ yr for Super earth.

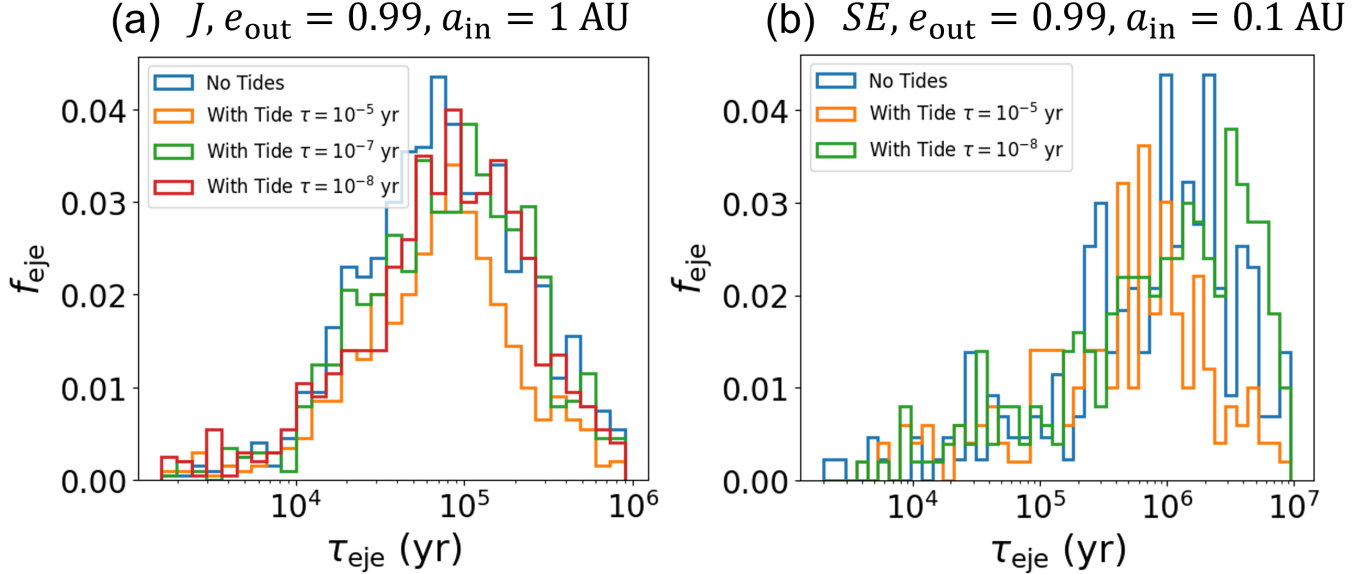


Figure 7. The ejection fraction analysis for Jupiter ($m_{\text{out}} = m_{\text{in}} = M_J$ on the left panel) or super-Earth systems ($m_{\text{out}} = m_{\text{in}} = 10M_{\oplus}$ on the right panel). Here, $e_{\text{in}} = 0$, $a_{\text{out}} = 10$ au, $e_{\text{out}} = 0.99$ and $a_{\text{in}} = 0.1$ au. The influence of tides on the ejection probability for Jupiter remains very limited.

4.1. Tidal disruption

Planets disintegrate when their periastron is reduced below their tidal disruption distance

$$d_{\text{TDE}} = 1.05(M_{\star}/\rho_p)^{1/3} = 1.7R_{\star}(\rho_{\star}/\rho_p)^{1/3}, \quad (18)$$

where ρ_{\star} and ρ_p are the average density of the star and planet, respectively (Sridhar & Tremaine 1992). For a Sun-like star, $\rho_{\star} \simeq \rho_p$ for a Jupiter-mass planet and is about 0.25 times that of Earth. These density ratios imply $d_{\text{TDE}} \simeq 1.7R_{\odot}$ and R_{\odot} for Jupiter and Earth respectively. We classify gas giants with $R_{\star} < r_{\text{peri}} \lesssim d_{\text{TDE}}$ as planet-star mergers. Due to severe tidal perturbations, gas giants with r_{peri} slightly larger than d_{TDE} may still be disrupted after their first survivable stellar encounters (Liu et al. 2013). We note that our model does not include tidal inflation of gas giants during circularization (Gu et al. 2003), which could increase their radius, reduce density, enlarge d_{TDE} , and further enhance the merger rate.

4.2. Gas giant systems

Our REBOUNDx simulations spanning 1 Myr reveal tidal influences when comparing dissipative and non-dissipative regimes. For the $m_{\text{in}} = m_{\text{out}} = M_J$ gas giant model (left panel Fig. 7), gravitational ejections dominate the outcomes, occurring in 80% of cases for outer planets, while inner planet ejections remain exceptionally rare (Table 1). This large difference is due to the outer planet has much smaller initial semi-major axis and total energy per unit mass than the inner planets. Collisions occur in $\sim 20\%$ of the systems, with more than two-thirds of these collision cases involving coalescence with the Sun (Fig. 6). Among these, collisions between the inner planet and the Sun constitute the majority.

In principle, tidal interactions modify these evolutionary pathways. When the tidal effects are included, planets' rate of direct stellar impact is reduced by $\sim 5\%$ while their frequency of intrusion into the host stars' d_{TDE} is increased by $\sim 10\%$. The outer planet ejection probabilities remain nearly the same. Tidal dissipation inside the planets and their host stars also induces orbital decay, steering the outer planets toward stellar collisions or tidal disruption. But at least for this case, there are still a significant number of ejection cases that shows the feasibility of producing a free-floating Jupiter through this mechanism is not significantly suppressed by the tidal dissipation.

4.3. Super-Earth systems

For the super-Earth systems ($m_{\text{out}} = m_{\text{in}} = 10M_{\oplus}$) with the same orbital elements, the tide-free ejection fraction decreases greatly (Table 1), indicating that high ejection probability (53%) remains though slightly lower than that for Jupiter-mass systems. The ejection probability is slightly reduced ($\sim 10\%$) in models which include the tidal effects. Since $d_{\text{TDE}} \simeq R_{\star}$ for these high- ρ_p planets, the stellar collision is not enhanced by the tidal disruption process. Moreover, orbital evolution due to tidal dissipation in these planets and their host stars remains weak.

We also consider a systems with $e_{\text{out}} = 0.999$ and the initial pericenter distance of the outer planets $r_{\text{peri,out}} = 0.01\text{au} = 2R_{\star}$). The super-Earth ejection probability from tide-free scattering remains high ($\sim 52\%$). However, with the tidal effect, the ejection probability decreases by a factor of $\gtrsim 2$ (Table 1) despite $d_{\text{TDE}} = R_{\star}$. This reduction is accompanied by a large increase in the planet-star merger rate. With τ_e being a steeply increasing function of either $r_{\text{peri,in}}$ or $r_{\text{peri,out}}$ (Eq. 15), tidal influence on their semi major axis and eccentricity evolution intensifies (Eqs. A24 and A25) for close-in planets and their host stars. Planets with such small periastron distances undergo orbital decay on a timescale shorter than the von Zeipel-Lidov-Kozai (vZLK) timescale ($\tau_e \lesssim \tau_{\text{vZLK}}$, §2.3), leading to prolific mergers with their host stars.

Table 1. Statistical frequencies of planetary ejection, merging, and retention across various models within 10 Myr evolution. Each model presents results for both tidal (+) and non-tidal (−) circumstances.

m_{out}	m_{in}	a_{out}	a_{in}	e_{out}	Tide	f_{eje}^1 (%)	$f_{\text{eje,in}}^2$ (%)
$10M_{\oplus}$	$10M_{\oplus}$	10	0.1	0.99	−	52.5 + 7.1	0.0
					+	36.3 + 28.8	0.0
$10M_{\oplus}$	$10M_{\oplus}$	10	0.1	0.999	−	51.5 + 4.2	0.0
					+	27.4 + 23.4	0.0
M_{J}	M_{J}	10	0.1	0.99	−	80.2 + 6.1	0.0
					+	77.4 + 3.2	0.02
M_{J}	$10M_{\oplus}$	10	0.1	0.99	−	6.5 + 32.1	0.0
					+	6.8 + 43.6	0.02

¹ Ejection rate of the intruder planet. Ejections include: 1) direct ejection during the simulation ($e_{\text{out}} > 1$ and $r_{\text{out}} > 1000$ au), and 2) cases where, at the time of the inner planetary merger, the intruder has achieved a hyperbolic orbit ($e_{\text{out}} > 1$) and is therefore destined for ejection (corresponding rates shown after the + sign).

² Ejection rate of the close-in planet.

5. ORBITS OF THE RETAINED POPULATION

We now examine the changes in orbital elements for planets that survive the dynamical instability. The outcomes are presented separately for systems where the outer planet is ejected and for those where a planet-star merger occurs. Planet-planet mergers are rare compared to planet-star mergers. Furthermore, if the outer planet collides with the star, the inner planet is typically also consumed, clearing the system entirely. Therefore, we focus on the subset of systems where only the inner planet is consumed. We analyze three model types: a) super-Earths only ($m_{\text{in}} = m_{\text{out}} = 10M_{\oplus}$), b) Jupiters only ($m_{\text{in}} = m_{\text{out}} = M_{\text{J}}$), and c) mixed systems ($m_{\text{in}} = 10M_{\oplus}$, $m_{\text{out}} = M_{\text{J}}$). All models have $a_{\text{out}} = 10$ au, $a_{\text{in}} = 0.1$ au, $e_{\text{in}} = 0$, and neglect tidal effects.

The lower panels of Fig. 8 show systems where the outer planet is ejected. Because the inner planet is more tightly bound, its ejection is far less likely than that of the outer planet ($f_{\text{eje,in}} \ll f_{\text{eje}}$, Table 1). The orbital energy conservation (Eq. 17) dictates that the surviving inner planets undergo significant modification, characterized by a reduction in their semi-major axes, a'_{in} , and excitation of their eccentricities. While these planets begin on circular orbits, the outcome is a broad eccentricity distribution with a prominent peak near 0.1. The model with $m_{\text{out}} = M_{\text{J}}$, $m_{\text{in}} = 10M_{\oplus}$ (bottom-right panel of Fig. 8) is a notable exception. Here, the exceptionally large energy exchange leads to a severe alteration of the semi-major axis and drives the average eccentricity to roughly 0.5. Inner planets with $a'_{\text{in}}(1 - e'_{\text{in}}) \leq R_{\star}$ merge with the host stars. Subsequent tidal circularization would further reduce a_{in} , potentially forming ultrashort-period planets.

The ejection process also randomizes orbital inclinations. While the inner planets begin in a coplanar disk aligned with the stellar spin, the gravitational interaction with the ejected outer planet leaves the survivors with a nearly uniform inclination distribution, including retrograde orbits (Fig. 8, yellow to blue dots). This implies the generation of a broad star-planet obliquity distribution. This mechanism is a variant of the conventional scenario for spin-orbit misalignment, which typically invokes the vZLK effect on single-planet systems (Wu & Murray 2003). The existence of planets on retrograde, nearly parabolic orbits with small inclinations could thus serve as dynamical fossils, indicating a past FFP ejection event.

We next consider changes to the outer planet’s orbit following the merger of the inner planet with the host star. The upper panels of Fig. 8 reveal distinct outcomes:

- In Jupiter-only systems (model b), the most common outcomes are the ejection of the outer planet or the consumption of both planets by the star. Very few single planets survive the merger of their partner with the host star.
- A larger fraction of super-Earth systems (model a) produce single survivors after the inner planets merge with the host stars.
- In mixed systems (model c), the mergers of the inner super-Earths with the stars significantly alter the orbits of the outer gas giants in approximately half of the cases.

The semi-major axes of the surviving outer planets are dispersed widely from their initial values (open black stars in Fig. 8). As the inner planet loses angular momentum to collide with the star, the outer planet can either gain or lose orbital energy during its close encounters, leading to either an increase or decrease in a_{out} . This angular momentum exchange also circularizes the outer planet’s orbit, reducing its eccentricity from the initial value of 0.99, though the final eccentricities still cluster near unity. The initial inclination distribution of the survivors is largely preserved.

6. ESTIMATED CONTRIBUTION TO THE FREE-FLOATING PLANET POPULATION

Of Sun-like stars, about $\sim 30\%$ (P_{SE}) host inner super-Earths (SE) and roughly $\sim 10\%$ (P_{CJ}) host a cold Jupiter (CJ). Studies indicate that nearly $\sim 90\%$ of cold Jupiters are expected to have interior small planets (Zhu & Wu 2018; Bryan et al. 2019). Among these inner super-Earths, approximately one-third are hot super-Earths (HSE, $R_{\text{in}} < 4R_{\oplus}$) with orbital periods $P_{\text{in}} < 10$ days. Based on transit and radial-velocity samples, it is estimated that about 40% of Sun-like stars with a cold Jupiter also host a hot super-Earth (Liu, Zhu, et al. in prep), i.e. $P_{\text{HSE|CJ}} \approx 0.4$.

The observed occurrence rate of hot Jupiters (HJ) is around 1% (P_{HJ}) (Howard et al. 2012; Santerne et al. 2016). However, studies such as (Gan et al. 2023) report a lower rate of $\sim 0.2\%$ around M dwarfs. Hot Jupiters can form either via disk migration or high-eccentricity migration. We denote by c the fraction of hot Jupiters that form through the high-eccentricity migration channel. If we assume that they form exclusively via the high-eccentricity migration channel ($c \approx 1$), thus only those cold Jupiters that do not harbor an inner hot super-Earth can be excited to high eccentricity by external perturbers—a process independent of the inner system—then the fraction of cold Jupiters that undergo such excitation, f_{He} , can be approximated by

$$cP_{\text{HJ}} = P_{\text{CJ}} \times (1 - P_{\text{HSE|CJ}}) \times f_{\text{He}}. \quad (19)$$

Inserting the observational values yields $f_{\text{He}} \approx 0.01/[0.1 \times (1 - 0.4)] \approx 17\%$. This estimate is consistent with the simulation results obtained by Ochiai et al. (2014). Their simulations show that, among cold Jupiters experiencing orbital instability, approximately 15 – 20% undergo eccentricity excitation to $e \sim 1$. Consequently, if the fraction of cold Jupiters that undergo orbital instability is $\sim 50 – 80\%$, the resulting fraction f_{He} is estimated to be $\sim 7.5 – 16\%$.

Using this excitation rate, we can then estimate the production rate of free-floating Jupiters (FFJs) through close encounters between excited cold Jupiters and inner hot super-Earths:

$$P_{\text{FFJ}} = P_{\text{CJ}} \times P_{\text{HSE|CJ}} \times f_{\text{He}} \times f_{\text{eje}}, \quad (20)$$

where f_{eje} is the ejection fraction during such encounters. According to Ochiai et al. (2014), the ejection rate of cold Jupiter without an inner super-Earth is 40%–60%. Based on our results, assuming the ejection frequency of cold Jupiter with a close-in super-Earth is nearly certain ($f_{\text{eje}} \approx 1$) in this regime, the resulting FFP production rate is $\approx 0.7\%$.

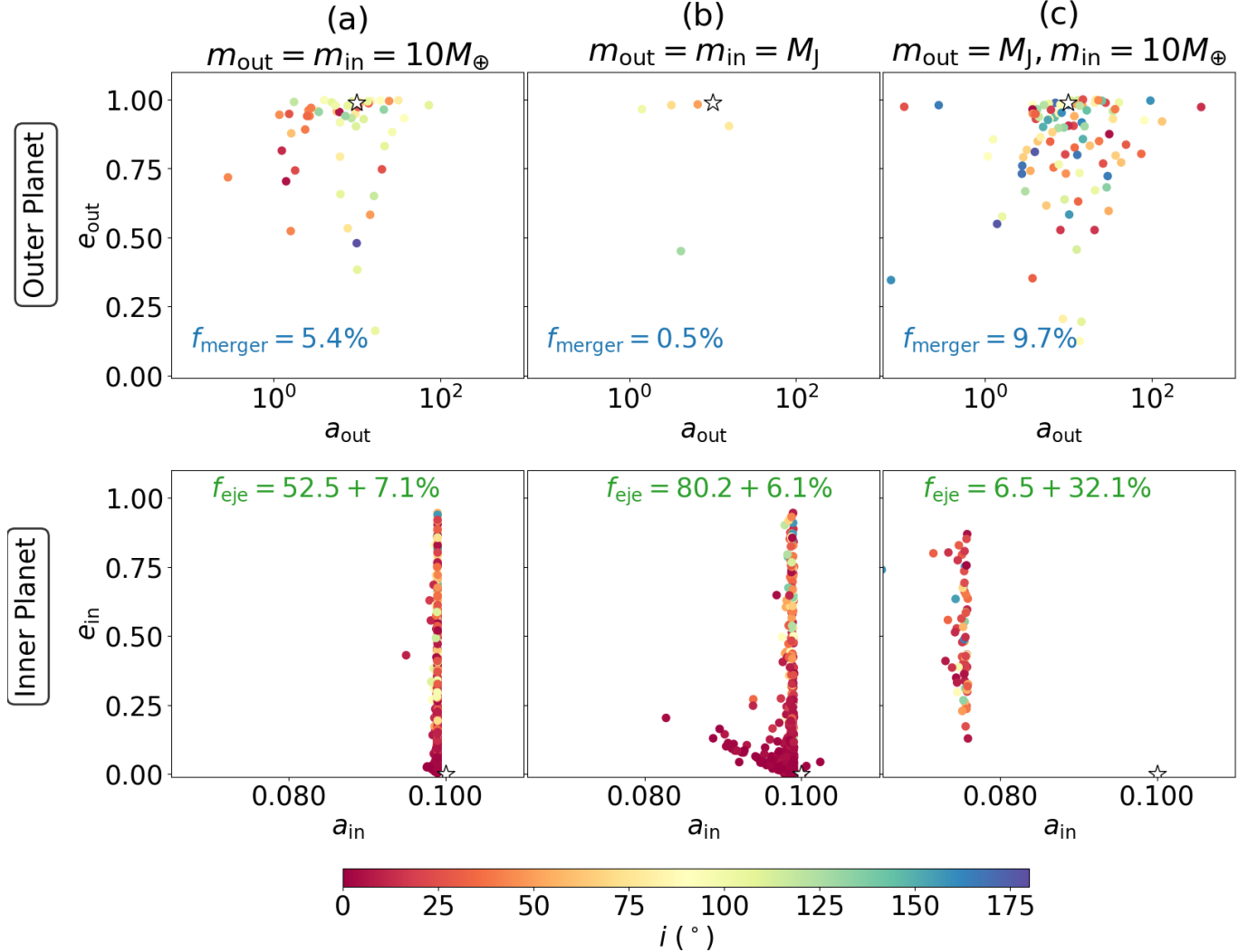


Figure 8. **Top Panels:** Final orbital elements of the outer planet remaining after the merger of its close-in companion with the host star. **Bottom Panels:** Final orbital elements of the close-in planet remaining after the ejection of the outer planet. All three configurations share the following initial conditions: an outer planet semi-major axis of $a_{\text{out}} = 10$ au ($= 100 a_{\text{in}}$), an outer planet eccentricity of $e_{\text{out}} = 0.99$, and an inner planet eccentricity of $e_{\text{in}} = 0$. The panels vary the planetary mass ratios, **Left (a):** $m_{\text{out}} = m_{\text{in}} = 10M_{\oplus}$; **Center (b):** $m_{\text{out}} = m_{\text{in}} = M_J$; **Right (c):** $m_{\text{out}} = M_J, m_{\text{in}} = 10M_{\oplus}$. The top panels are annotated with the fraction (f_{merger}) of simulations where the inner planet merged with the host star. The bottom panels show the ejection fraction (f_{eje}) of the outer planet. The initial conditions for each planet are marked by an open black star in its respective final-state panel. Color bars indicate the final inclination of the outer planet (top) and the inner planet (bottom). Red dashed line (bottom) indicates the limit for R_{\star} interception.

However, this FFJ production rate applies only to objects of Jovian mass. To extrapolate this rate to the total population of free-floating planets, we must consider the complete mass distribution of cold planets derived from microlensing surveys (Zang et al. 2025):

$$\frac{dN}{d \log q} = f(\log q), \quad \text{where} \quad f(\log q) \approx 0.52 \times 10^{-0.73 \times (\log q / 7.4q_{\oplus})^2} + 0.058 \times 10^{-1.8 \times (\log q / 770q_{\oplus})^2}. \quad (21)$$

Within this distribution, cold Jupiters (defined here as objects with masses between Saturn's mass and $13 M_J$) constitute only a small fraction of the total cold-planet population. This fraction, $P_{\text{CJ}}/P_{\text{CP}}$, is given by:

$$\frac{P_{\text{CJ}}}{P_{\text{CP}}} = \frac{\int_{\log(M_{\text{Sat}}/M_{\odot})}^{\log(13M_J/M_{\odot})} f(\log q) d\log q}{\int_{-6}^{-1.5} f(\log q) d\log q} \approx 0.085. \quad (22)$$

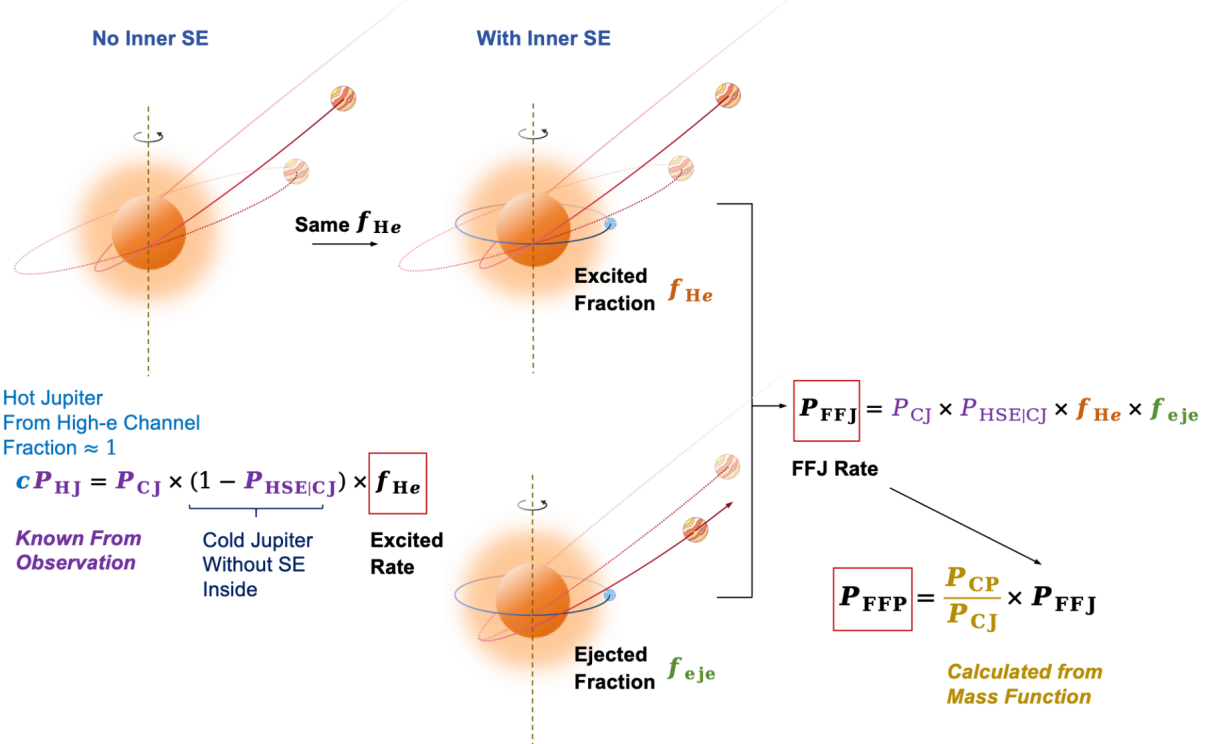


Figure 9. A flowchart illustrating the methodology for estimating the approximate production rate of FFPs (free-floating planets). First, the excitation frequency of cold Jupiters is estimated using systems containing a cold Jupiter but no inner super-Earth. This frequency is assumed to be identical for cold Jupiter systems with an inner super-Earth. Subsequently, the estimated FFJ (free-floating Jupiter) production rate is derived. Finally, by applying the mass function to obtain the ratio of cold planets to cold Jupiters, the overall FFP production rate is calculated.

The occurrence rate of cold Jupiters around M dwarfs is approximately one-fourth of the corresponding frequency inferred for such planets orbiting FGK stars (Clanton & Gaudi 2014; Montet et al. 2014; see also Gan et al. 2024). Therefore, for an order-of-magnitude estimate, the occurrence rate for M dwarfs may serve as a reasonable approximation for that of Sun-like stars. Furthermore, population-synthesis studies utilizing a realistic IMF and microlensing constraints support the plausibility of high ejection efficiencies also in M-dwarf-dominated stellar populations (Guo et al. 2025).

Guo et al. (2025) concluded that the dominant population contributing to the free-floating planet population are planets of Neptune-like masses. The estimated total free-floating planet production rate arises from dynamical encounters between cold planets (across all masses) and close-in super-Earths. This rate can therefore be scaled from the free-floating Jupiter (P_{FFJ}) rate as follows:

$$P_{FFP} = P_{FFJ} \times \frac{P_{CP}}{P_{CJ}} \approx 8\%. \quad (23)$$

Finally, it is important to note that this estimate is conservative. It is derived specifically from interactions involving the observed populations of close-in super-Earths and cold planets. In reality, other populations—such as hot Neptunes and even hot Jupiters—can also eject cold planets, potentially contributing to a higher overall FFP production rate than calculated here.

7. SUMMARY AND DISCUSSIONS

Recent microlensing surveys indicate that freely floating planets (FFPs) may outnumber known bound planets. This work explores a viable formation channel for FFPs arising from gravitational encounters between distinct planetary populations within a planetary system.

Our study focuses specifically on the post-gas-disk phase, when the gas disk is severely depleted or absent. At this stage, high-eccentricity tidal migration of cold Jupiters is a leading scenario for forming hot Jupiters. We adopt this

established framework as our starting point, asking a subsequent question: if such a highly eccentric giant planet progenitor exists, what is the dynamical fate of such a planetary system that already hosts close-in planets?

Close-in planets are likely to have formed at larger orbital distances and subsequently migrated to their current locations via disk migration (Lin et al. 1996) or high-eccentricity migration (Wu & Murray 2003). High-eccentricity migration, in particular, proposes that these planets were injected toward the star by perturbations from distant companions, through mechanisms such as the von Zeipel–Lidov–Kozai (vZLK) effect, sweeping secular resonances, or secular chaos (Ida & Lin 2004).

Our work investigates a logical outcome of such dynamical processes: when multiple planets are driven to small periastron distances, or when a long-period intruding planet enters the orbital region of existing close-in planets, their orbits may intersect. During close encounters, strong two-body scattering can take place. Since the intruding planet possesses significantly lower orbital energy per unit mass ($-GM_*/2a$) than the close-in planets, even a modest fractional energy exchange can lead to the ejection of the intruder from the system, forming an FFP. We analyze this FFP-formation channel using both analytical estimates (§2.2) and numerical simulations (§3). Our results demonstrate that such interactions provide an efficient and robust mechanism for the production of free-floating planets.

On the technical side, this paper analyzes the energy exchange during close encounters between intruding cold planets and close-in planets. Using an impulse approximation, we derive an analytic expression for the critical impact parameter that leads to significant energy exchange and potential ejection. This quantity (Eq. 9) depends on the inner planet’s mass (m_{in}) and the outer planet’s semi-major axis (a_{out}), but is independent of a_{in} and m_{out} . Consequently, under certain conditions:

- Close encounters with short-period super-Earths can eject more massive, long-period gas giants.

This analytical prediction is validated by numerical simulations (§3), which demonstrate that both the ejection timescales and frequencies depend on the planetary mass ratio and the semi-major axis of the close-in planet (Fig. 5), consistent with the theoretical framework in §2.2. We further find that:

- As inner planets, hot Jupiters are able to eject nearly all intruding long-period planets (Table 1).

This result implies that the presence of hot Jupiters would prevent the implantation of nearby planets through high-eccentricity migration. Any closely-packed multiple planets in the vicinity of hot Jupiters, if they exist, must have acquired their present-day orbital configurations through disk migration.

Close-in ($a_{\text{in}} \leq 0.1$ au) super-Earths are significantly more common than hot Jupiters.

- They also exhibit a high probability of ejecting intruding cold super-Earths (Fig. 4).

Comets greatly outnumber planets. In a subsequent study, we will demonstrate that their ejection via close encounters with close-in super-Earths provides a robust production mechanism for interstellar comets and asteroids (Zhang & Lin 2020). When their dynamical domain is encroached by cold gas giants,

- close-in super-Earths become vulnerable to e_{in} -excitation and are susceptible to stellar merger (Fig. 6).

Profuse stellar consumption of super-Earths can produce observable abundance dispersions among stars in young clusters (Shen et al. 2005) and metallicity differences in binary systems (González Hernández et al. 2013; Liu et al. 2014; Saffe et al. 2019).

- The substantial depletion of close-in super-Earths consequently reduces their efficiency in ejecting gas giants (Table 1).

The preferential ejection probability of intruding cold super-Earths over gas giants aligns with the mass distribution of free-floating planets (FFPs) inferred from microlensing surveys. In addition to stellar collisions, super-Earths exhibit the following behavior:

- Close-in super-Earths have a small but non-negligible probability of undergoing mergers with intruding gas giants (Table 1).

Planetary mergers can contribute to the diversity in the internal structures of gas giant planets (Liu et al. 2015, 2019). Although tidal dissipation and disruption can increase the likelihood of mergers (§2.3 and §4),

- the ejection mechanism described here remains a viable formation channel for FFPs (Fig. 7).

Following the ejection of the outer planets, the orbital elements of the surviving inner planets exhibit significant modifications:

- their eccentricities become markedly excited, in some cases reaching retrograde configurations; and
- their semi-major axes experience a fractional decrease (lower panel of Fig. 8).

Both outcomes consequently induce subsequent tidal orbital evolution. A natural extension of this work is to investigate the stability and potential disintegration of multiple close-in super-Earth systems when perturbed by intruding super-Earths and gas giants.

In models where the inner planets experience collisions with their host star, the orbital parameters of the surviving outer planets undergo systematic modifications:

- their semi-major axes spread out by approximately a factor of two; and
- their eccentricities are reduced by up to a factor of two (upper panel of Fig. 8).

In a subsequent investigation, we intend to examine systems with long-period inner planets and explore whether their close encounters with long-period gas giants on nearly parabolic orbits could lead to the formation of eccentric warm Jupiters. Within this post-disk context, the presence of a close-in super-Earth—a common outcome of in-situ formation or disk migration—can efficiently halt high-eccentricity migration. Through strong gravitational scattering, it can eject the incoming giant planet, thereby protecting the inner terrestrial environment and contributing to the free-floating planet population. This result highlights a critical constraint on the high-eccentricity migration channel. We explore implications for the observed orbital alignments of warm and hot Jupiters further in a follow-up study (Cao et al., in prep).

We thank Drs. Tianjun Gan, Wei Zhu, and Weicheng Zang for useful discussions. The authors acknowledge the Tsinghua Astrophysics High-Performance Computing platform at Tsinghua University for providing computational and data storage resources that have contributed to the results in this paper. XCZ is supported by the National Natural Science Foundation of China (Grant No. 12203007) and the Mengya Program of Beijing Academy of Science and Technology (BGS202203). ZYC and SM are partly supported by the National Science Foundation of China (Grant No. 12133005).

Software: REBOUNDx (Tamayo et al. 2020), REBOUND (Rein & Liu 2011), Kozaipy (<https://github.com/djmunoz/kozaipy>)

APPENDIX

A. TIDAL DISSIPATION THEORY ANALYSIS

The force responsible for tidal dissipation in the planet and star includes two parts:

$$\mathbf{F}_{\text{tidal}} = F_r \hat{\mathbf{e}}_r + F_\theta \hat{\mathbf{e}}_\theta \quad \text{with} \quad (A1)$$

$$F_r = -3G \frac{m^2}{r^2} \frac{R^5}{r^5} k \left(1 + 3 \frac{\dot{r}}{r} \tau \right), \quad F_\theta = 3G \frac{m^2}{r^2} \frac{R^5}{r^5} k \tau \left(\Omega - \dot{\theta} \right), \quad (A2)$$

where Ω is the spin rate of the deformed body. For a planet (or a star) as the deformed body and its stellar (or planetary companion) as the perturbing body, $M = M_{p,*}$, $m = M_{*,p}$, $q \equiv M/m = M_{p,*}/M_{*,p}$, $\Omega = \Omega_{p,*}$, $R = R_{p,*}$, $k = k_2^{p,*}$, and $\tau = \tau_{\text{lag}}^{p,*}$, respectively. In the present context, we consider the nearly parabolic planet as the deformed body and its host star as the tidal perturbing body (with $m = M_p$ and $M = M_*$). Since the influence of each orbital tide constitutes a minor perturbation, the effects of tidal forces can be decomposed into the radial and azimuthal components for separate analysis, followed by linear superposition. The variations induced by F_r are denoted by \dot{a}_r

and \dot{e}_r , while those caused by F_θ are represented as \dot{a}_θ and \dot{e}_θ . According to [Hut \(1981\)](#), both a_r and a_θ as well as e_r and e_θ components contribute to the changing rate of eccentricity and semi-major axis, respectively:

$$\dot{a} = \dot{a}_r + \dot{a}_\theta \quad \text{and} \quad \dot{e} = \dot{e}_r + \dot{e}_\theta. \quad (\text{A3})$$

We first consider the force in the radial direction. At radial distance from the star and the radial velocity are

$$r = a \frac{(1 - e^2)}{(1 + e \cos \theta)}, \quad \dot{r} = r \frac{e \sin \theta}{(1 + e \cos \theta)} \dot{\theta} = \sqrt{\frac{G(M+m)}{a(1-e^2)}} e \sin \theta. \quad (\text{A4})$$

The total angular momentum is given by

$$h = \frac{Mmr^2}{(M+m)} \dot{\theta}, \quad \text{with} \quad h^2 = G \frac{M^2 m^2}{(M+m)} a(1 - e^2). \quad (\text{A5})$$

Energy change is calculated as

$$\begin{aligned} \Delta E_r &= \int_{\delta t}^{\Delta\theta} F_r dr = \int_{-\Delta\theta}^{\Delta\theta} F_r \frac{dr}{d\theta} d\theta = \int_{-\Delta\theta}^{\Delta\theta} F_r a \frac{e(1-e^2)}{(1+e\cos\theta)^2} \sin\theta d\theta \\ &= \int_{-\Delta\theta}^{\Delta\theta} (-9G) \frac{m^2}{r^2} \left(\frac{R}{r}\right)^5 k \frac{\dot{r}}{r} \tau a \frac{e(1-e^2)}{(1+e\cos\theta)^2} \sin\theta d\theta \\ &= -9Gm^2 R^5 k \tau a e (1-e^2) \int_{-\Delta\theta}^{\Delta\theta} \frac{\dot{r} \sin\theta}{r^8 (1+e\cos\theta)^2} d\theta. \end{aligned} \quad (\text{A6})$$

Since the magnitude of ΔE decreases steeply with r , we adopt the integration interval $\Delta\theta = \pi/2$ for computational convenience. For nearly parabolic orbit with $e = 1 - \epsilon$ and $\epsilon \ll 1$, $r(\theta = \pi/2) \simeq 2r_{\text{peri}}$ where r_{peri} is the peri-apsis distant $r_{\text{peri}} = a(1 - e) = \epsilon a$. Integration beyond this range of $\Delta\theta$ would modify the magnitude of ΔE by $\lesssim 2\%$. With this approximation,

$$\begin{aligned} \Delta E_r &\simeq -9G^{\frac{3}{2}} m^2 R^5 k \tau e^2 \frac{(M+m)^{1/2}}{(1-e^2)^{15/2} a^{15/2}} \int_{-\pi/2}^{\pi/2} \sin^2\theta (1+e\cos\theta)^6 d\theta \\ &= -9f_1(e) G^{\frac{3}{2}} m^2 R^5 k \tau e^2 \frac{(M+m)^{1/2}}{(1-e^2)^{15/2} a^{15/2}}, \\ \text{where} \quad f_1(e) &= \frac{\pi}{2} + 4e + \frac{15\pi}{8}e^2 + \frac{16}{3}e^3 + \frac{15\pi}{16}e^4 + \frac{32}{35}e^5 + \frac{5\pi}{128}e^6. \end{aligned} \quad (\text{A7})$$

To calculate the rate of E_r change, we use the average rate over the period, $P = 2\pi/n$ where $n = \sqrt{G(M+m)/a^3}$ is the mean motion,

$$\dot{E}_r \simeq \frac{\Delta E_r}{P} = -\frac{9f_1(e)}{2\pi} G^2 m^2 R^5 k \tau e^2 \frac{(M+m)}{(1-e^2)^{15/2} a^9}. \quad (\text{A8})$$

Based on the total energy $E = -GMm/2a$, we can calculate the rate of change in semi-major axis \dot{a}_r due to F_r such that

$$\dot{a}_r = \frac{2a^2 \dot{E}_r}{GMm} = -\frac{9f_1(e)}{\pi} GR^5 k \tau e^2 \frac{m(M+m)}{M(1-e^2)^{15/2} a^7}. \quad (\text{A9})$$

Since F_r does not lead to any angular momentum changes, we find from (A5):

$$\begin{aligned} 2h\dot{h} &= G \frac{M^2 m^2}{(M+m)} [\dot{a}_r(1-e^2) - 2ae\dot{e}_r] = 0 \\ \Rightarrow \dot{e}_r &= \frac{\dot{a}_r(1-e^2)}{2ae} = -\frac{9f_1(e)}{2\pi} GR^5 k \tau e \frac{m(M+m)}{M(1-e^2)^{13/2} a^8}. \end{aligned} \quad (\text{A10})$$

In sum, for \hat{r} direction, replacing e with $1 - \epsilon$ and only considering the first order of ϵ , we get

$$\begin{aligned}\dot{a}_r &\simeq \frac{-9g_{11}(\epsilon)}{128\sqrt{2}\pi} GR^5 k\tau \frac{m(M+m)}{M\epsilon^{15/2}a^7}, \\ \dot{e}_r &\simeq -\frac{9g_{12}(\epsilon)}{128\sqrt{2}\pi} GR^5 k\tau \frac{m(M+m)}{M\epsilon^{13/2}a^8},\end{aligned}\quad (\text{A11})$$

where

$$\begin{aligned}g_{11}(\epsilon) &\simeq \frac{1076}{105} + \frac{429\pi}{128} - \left(\frac{676}{15} + \frac{231\pi}{16} \right) \epsilon, \\ g_{12}(\epsilon) &\simeq \frac{1076}{105} + \frac{429\pi}{128} - \left(\frac{3656}{105} + \frac{1419\pi}{128} \right) \epsilon.\end{aligned}\quad (\text{A12})$$

Next, we consider the $\hat{\theta}$ direction,

$$\begin{aligned}\Delta E_\theta &= \int_{-\Delta\theta}^{\Delta\theta} r F_\theta d\theta \simeq 3Gm^2 R^8 k\tau \int_{-\pi/2}^{\pi/2} \frac{(\Omega - \dot{\theta})}{r^7} d\theta \\ &= 3 \frac{k}{T} \frac{m^2}{M} \frac{R^8}{a^6 (1-e^2)^6} \int_{-\pi/2}^{\pi/2} \left[(1+e\cos\theta)^6 \Omega - \frac{(1+e\cos\theta)^8}{(1-e^2)^{3/2}} n \right] d\theta \\ &= 3 \frac{k}{T} \frac{m^2}{M} \frac{R^8}{a^6 (1-e^2)^6} \left[f_2(e)\Omega - \frac{f_3(e)}{(1-e^2)^{3/2}} n \right],\end{aligned}\quad (\text{A13})$$

where $T = R^3/GM\tau = ((M+m)/Mn^2\tau)(R^3/a^3)$,

$$\begin{aligned}f_2(e) &= \pi + 12e + \frac{15\pi}{2}e^2 + \frac{80}{3}e^3 + \frac{45\pi}{8}e^4 + \frac{32}{5}e^5 + \frac{5\pi}{16}e^6, \\ f_3(e) &= \pi + 16e + 14\pi e^2 + \frac{224}{3}e^3 + \frac{105\pi}{4}e^4 + \frac{896}{15}e^5 + \frac{35\pi}{4}e^6 + \frac{256}{35}e^7 + \frac{35\pi}{128}e^8.\end{aligned}\quad (\text{A14})$$

From the time-averaged rate of change in E_θ ,

$$\dot{E}_\theta = \frac{\Delta E_\theta}{P} = \frac{3}{2\pi} \frac{nk}{T} \frac{m^2}{M} \frac{R^8}{a^6 (1-e^2)^6} \left[f_2(e)\Omega - \frac{f_3(e)}{(1-e^2)^{3/2}} n \right], \quad (\text{A15})$$

we derive

$$\begin{aligned}\dot{a}_\theta &= \frac{2a^2 \dot{E}_\theta}{GMm} \\ &= \frac{3}{\pi} \frac{k}{nT} \frac{m(M+m)}{M^2} \frac{R^8}{a^7 (1-e^2)^6} \left[f_2(e)\Omega - \frac{f_3(e)}{(1-e^2)^{3/2}} n \right].\end{aligned}\quad (\text{A16})$$

For nearly parabolic orbits (with $\epsilon \ll 1$), the perigee distance $r_p = (1-e)a \simeq \epsilon a$. Its rate of fractional changes $\dot{r}_p/r_p = \dot{a}/a - \dot{e}/(1-e)$ is dominated by changes in e . In order to derive an expression for \dot{e} , we first obtain from eq.(A5),

$$\dot{\theta} = \frac{\sqrt{aG(1-e^2)(M+m)}}{r^2} = n \frac{(1+e\cos\theta)^2}{(1-e^2)^{3/2}}, \quad (\text{A17})$$

$$\begin{aligned}\Delta h_\theta &= \int_{-\Delta\theta}^{\Delta\theta} r F_\theta \frac{d\theta}{\dot{\theta}} = -\frac{3}{(1-e^2)^6} \frac{k}{T} \frac{m^2}{M} \frac{R^8}{a^6} \int_{-\Delta\theta}^{\Delta\theta} \left[(1+e\cos\theta)^6 - (1-e^2)^{3/2} (1+e\cos\theta)^4 \frac{\Omega}{n} \right] d\theta \\ &= -\frac{3}{(1-e^2)^6} \frac{k}{T} \frac{m^2}{M} \frac{R^8}{a^6} \left[f_2(e) - (1-e^2)^{3/2} f_4(e) \frac{\Omega}{n} \right],\end{aligned}\quad (\text{A18})$$

where

$$f_4(e) = \pi + 8e + 3\pi e^2 + \frac{16}{3}e^3 + \frac{3\pi}{8}e^4. \quad (\text{A19})$$

Averaging over the orbital period P ,

$$\begin{aligned}\dot{h}_\theta &= \frac{\Delta h_\theta}{P} \\ &= -\frac{3}{2\pi(1-e^2)^6} \frac{nk}{T} \frac{m^2}{M} \frac{R^8}{a^6} \left[f_2(e) - (1-e^2)^{3/2} f_4(e) \frac{\Omega}{n} \right].\end{aligned}\tag{A20}$$

Substitute \dot{a}_θ in Eq. (A16) into Eq. (A5), we find

$$\begin{aligned}\dot{e}_\theta &= \frac{1}{2} \frac{(1-e^2)}{ae} \dot{a}_\theta - \frac{(M+m)h}{GM^2 m^2 ae} \dot{h}_\theta \\ &= \frac{3}{2\pi} \frac{k}{nT} \frac{m(M+m)}{M^2} \frac{R^8}{a^8 e (1-e^2)^5} \left[f_2(e)\Omega - \frac{f_3(e)}{(1-e^2)^{3/2}} n \right] \\ &\quad - \frac{3}{2\pi} \frac{k}{nT} \frac{m(M+m)}{M^2} \frac{R^8}{a^8 e (1-e^2)^4} \left[\frac{f_2(e)}{(1-e^2)^{3/2}} n - f_4(e)\Omega \right].\end{aligned}\tag{A21}$$

Replacing e with $1-\epsilon$, we get

$$\begin{aligned}\dot{a}_\theta &= \frac{3}{128\pi} \frac{k}{nT} \frac{m(M+m)}{M^2} \frac{R^8}{a^7 \epsilon^6} \left[g_{21}(\epsilon)\Omega - \frac{g_{31}(\epsilon)}{2\sqrt{2}\epsilon^{3/2}} n \right], \\ \dot{e}_\theta &= \frac{3}{64\pi} \frac{k}{nT} \frac{m(M+m)}{M^2} \frac{R^8}{a^8 \epsilon^5} \left[g_{22}(\epsilon)\Omega - \frac{g_{32}(\epsilon)}{2\sqrt{2}\epsilon^{3/2}} n \right] \\ &\quad - \frac{3}{32\pi} \frac{k}{nT} \frac{m(M+m)}{M^2} \frac{R^8}{a^8 \epsilon^4} \left[\frac{g_{22}(\epsilon)}{2\sqrt{2}\epsilon^{3/2}} n - g_{42}(\epsilon)\Omega \right],\end{aligned}\tag{A22}$$

where

$$\begin{aligned}g_{21}(\epsilon) &\simeq \frac{676}{15} + \frac{231\pi}{16} - (124 + \frac{315\pi}{8})\epsilon, \\ g_{31}(\epsilon) &\simeq \frac{1104}{7} + \frac{6435\pi}{128} - (\frac{8848}{15} + \frac{3003\pi}{16})\epsilon, \\ g_{22}(\epsilon) &\simeq \frac{676}{15} + \frac{231\pi}{16} - (\frac{1184}{15} + \frac{399\pi}{16})\epsilon, \\ g_{32}(\epsilon) &\simeq \frac{1104}{7} + \frac{6435\pi}{128} - (\frac{45376}{105} + \frac{17589\pi}{128})\epsilon, \\ g_{42}(\epsilon) &\simeq \frac{40}{3} + \frac{35\pi}{8} - (\frac{32}{3} + \frac{25\pi}{8})\epsilon.\end{aligned}\tag{A23}$$

The total rate of change

$$\begin{aligned}\dot{a} &= \dot{a}_r + \dot{a}_\theta \simeq \frac{-9g_{11}(\epsilon)}{128\sqrt{2}\pi} \frac{k}{T} \frac{m(M+m)}{M^2} \frac{R^8}{a^7 \epsilon^{15/2}} \\ &\quad + \frac{3}{128\pi} \frac{k}{nT} \frac{m(M+m)}{M^2} \frac{R^8}{a^7 \epsilon^6} \left[g_{21}(\epsilon)\Omega - \frac{g_{31}(\epsilon)}{2\sqrt{2}\epsilon^{3/2}} n \right] \quad \text{and}\end{aligned}\tag{A24}$$

$$\begin{aligned}\dot{e} &= \dot{e}_r + \dot{e}_\theta \simeq -\frac{9g_{12}(\epsilon)}{128\sqrt{2}\pi} \frac{k}{T} \frac{m(M+m)}{M^2} \frac{R^8}{a^8 \epsilon^{13/2}} \\ &\quad + \frac{3}{64\pi} \frac{k}{nT} \frac{m(M+m)}{M^2} \frac{R^8}{a^8 \epsilon^5} \left[g_{22}(\epsilon)\Omega - \frac{g_{32}(\epsilon)}{2\sqrt{2}\epsilon^{3/2}} n \right] \\ &\quad - \frac{3}{32\pi} \frac{k}{nT} \frac{m(M+m)}{M^2} \frac{R^8}{a^8 \epsilon^4} \left[\frac{g_{22}(\epsilon)}{2\sqrt{2}\epsilon^{3/2}} n - g_{42}(\epsilon)\Omega \right].\end{aligned}\tag{A25}$$

For physical interpretations, it is useful to recast the above expressions in terms of the dimensionless ratio $\tilde{R} \equiv R/R_R$ where $R_R = q^{1/3}r_{\text{peri}} = q^{1/3}a\epsilon$ is the planet's Roche radius at perigee, $q = M/m = M_p/M_\star$ is the planet to star mass ratio. It is also informative to introduce dimensionless response time, $\tilde{\tau}_\Omega = \Omega\tau$ where Ω is the planet's spin frequency and $\tilde{\tau}_n \equiv \tau/\Delta T$ where $\Delta T = P\epsilon^{3/2}$ is the time interval of perigee passage. These timescales are relevant to the

inertial-mode dynamical tides (Ogilvie & Lin 2004) and visco-elastic equilibrium tides (Remus et al. 2012). The first, second, and third terms in Eq (A25) become

$$\begin{aligned}\dot{e} = & -\frac{9\pi q^{2/3}}{32\sqrt{2}}\frac{k\tilde{\tau}_n}{P}\tilde{R}^5g_{12}(\epsilon) + \frac{3}{32}q^{2/3}\frac{k\tilde{\tau}_\Omega}{P}\tilde{R}^5\left[g_{22}(\epsilon) - \frac{\pi g_{32}(\epsilon)}{\sqrt{2}\Omega\Delta T}\right] \\ & - \frac{3}{16}\epsilon q^{2/3}\frac{k\tilde{\tau}_\Omega}{P}\tilde{R}^5\left[g_{42}(\epsilon) - \frac{\pi g_{22}(\epsilon)}{\sqrt{2}\Omega\Delta T}\right] \\ = & -q^{2/3}\frac{k\tilde{\tau}_n}{P}\tilde{R}^5\left\{\frac{9\pi g_{12}}{32\sqrt{2}} - \frac{3}{32}\left[g_{22}(\epsilon) - \frac{\pi g_{32}(\epsilon)}{\sqrt{2}\Omega\Delta T}\right] + \frac{3}{16}\epsilon\left[g_{42}(\epsilon) - \frac{\pi g_{22}(\epsilon)}{\sqrt{2}\Omega\Delta T}\right]\right\}.\end{aligned}\quad (\text{A26})$$

In principle $\Omega\Delta T > 1$ implies fast spin and eccentricity excitation (i.e. with $\dot{e}_\theta > 1$). In contrast, $\Omega\Delta T < 1$ implies slow spin and eccentricity damping (i.e. with $\dot{e}_\theta < 1$). The key point we wish to show is that the eccentricity evolution timescale

$$\tau_e = \frac{e}{\dot{e}} \propto \mathcal{O}\left(\frac{\epsilon P}{q^{2/3}k\tilde{\tau}_n\tilde{R}^5}\right). \quad (\text{A27})$$

is longer than the von Zeipel-Kozai-Lidov cycle and the ejection time scale (§2.3 and 4).

REFERENCES

Adams, F. C., Anderson, K. R., & Bloch, A. M. 2013, MNRAS, 432, 438, doi: [10.1093/mnras/stt479](https://doi.org/10.1093/mnras/stt479)

Andrews, S. M., Huang, J., Pérez, L. M., et al. 2018, ApJL, 869, L41, doi: [10.3847/2041-8213/aaf741](https://doi.org/10.3847/2041-8213/aaf741)

Asensio-Torres, R., Henning, T., Cantalloube, F., et al. 2021, A&A, 652, A101, doi: [10.1051/0004-6361/202140325](https://doi.org/10.1051/0004-6361/202140325)

Avenhaus, H., Quanz, S. P., Garufi, A., et al. 2018, ApJ, 863, 44, doi: [10.3847/1538-4357/aab846](https://doi.org/10.3847/1538-4357/aab846)

Baronett, S. A., Ferich, N., Tamayo, D., & Steffen, J. H. 2022, Monthly Notices of the Royal Astronomical Society, 510, 6001, doi: [10.1093/mnras/stac043](https://doi.org/10.1093/mnras/stac043)

Barrado y Navascués, D., Zapatero Osorio, M. R., Béjar, V., et al. 2002, in The Origin of Stars and Planets: The VLT View, ed. J. F. Alves & M. J. McCaughrean, 195, doi: [10.1007/10856518_24](https://doi.org/10.1007/10856518_24)

Béjar, V. J. S., Zapatero Osorio, M. R., & Rebolo, R. 1999, ApJ, 521, 671, doi: [10.1086/307583](https://doi.org/10.1086/307583)

Bhaskar, H., Li, G., Hadden, S., Payne, M. J., & Holman, M. J. 2021, AJ, 161, 48, doi: [10.3847/1538-3881/abcbfc](https://doi.org/10.3847/1538-3881/abcbfc)

Bryan, M. L., Knutson, H. A., Lee, E. J., et al. 2019, AJ, 157, 52, doi: [10.3847/1538-3881/aaf57f](https://doi.org/10.3847/1538-3881/aaf57f)

Clanton, C., & Gaudi, B. S. 2014, ApJ, 791, 91, doi: [10.1088/0004-637X/791/2/91](https://doi.org/10.1088/0004-637X/791/2/91)

Coleman, G. A. L., & DeRocco, W. 2025, MNRAS, 537, 2303, doi: [10.1093/mnras/staf138](https://doi.org/10.1093/mnras/staf138)

Coleman, G. A. L., Nelson, R. P., & Triaud, A. H. M. J. 2023, MNRAS, 522, 4352, doi: [10.1093/mnras/stad833](https://doi.org/10.1093/mnras/stad833)

Dai, F., Goldberg, M., Batygin, K., et al. 2024, AJ, 168, 239, doi: [10.3847/1538-3881/ad83a6](https://doi.org/10.3847/1538-3881/ad83a6)

Dong, S., & Zhu, Z. 2013, ApJ, 778, 53, doi: [10.1088/0004-637X/778/1/53](https://doi.org/10.1088/0004-637X/778/1/53)

Eggleton, P. P., Kiseleva, L. G., & Hut, P. 1998, ApJ, 499, 853, doi: [10.1086/305670](https://doi.org/10.1086/305670)

Everhart, E. 1985, in Astrophysics and Space Science Library, Vol. 115, IAU Colloq. 83: Dynamics of Comets: Their Origin and Evolution, ed. A. Carusi & G. B. Valsecchi, 185, doi: [10.1007/978-94-009-5400-7_17](https://doi.org/10.1007/978-94-009-5400-7_17)

Fabrycky, D., & Tremaine, S. 2007, ApJ, 669, 1298, doi: [10.1086/521702](https://doi.org/10.1086/521702)

Fabrycky, D. C., Lissauer, J. J., Ragozzine, D., et al. 2014, ApJ, 790, 146, doi: [10.1088/0004-637X/790/2/146](https://doi.org/10.1088/0004-637X/790/2/146)

Galicher, R., Marois, C., Macintosh, B., et al. 2016, A&A, 594, A63, doi: [10.1051/0004-6361/201527828](https://doi.org/10.1051/0004-6361/201527828)

Gan, T., Guo, K., Liu, B., et al. 2024, ApJ, 967, 74, doi: [10.3847/1538-4357/ad3deb](https://doi.org/10.3847/1538-4357/ad3deb)

Gan, T., Wang, S. X., Wang, S., et al. 2023, AJ, 165, 17, doi: [10.3847/1538-3881/ac9b12](https://doi.org/10.3847/1538-3881/ac9b12)

Garufi, A., Avenhaus, H., Pérez, S., et al. 2020, A&A, 633, A82, doi: [10.1051/0004-6361/201936946](https://doi.org/10.1051/0004-6361/201936946)

González Hernández, J. I., Delgado-Mena, E., Sousa, S. G., et al. 2013, A&A, 552, A6, doi: [10.1051/0004-6361/201220165](https://doi.org/10.1051/0004-6361/201220165)

Gould, A., Dong, S., Gaudi, B. S., et al. 2010, ApJ, 720, 1073, doi: [10.1088/0004-637X/720/2/1073](https://doi.org/10.1088/0004-637X/720/2/1073)

Gould, A., Jung, Y. K., Hwang, K.-H., et al. 2022, Journal of Korean Astronomical Society, 55, 173, doi: [10.5303/JKAS.2022.55.5.173](https://doi.org/10.5303/JKAS.2022.55.5.173)

Gu, P.-G., Lin, D. N. C., & Bodenheimer, P. H. 2003, ApJ, 588, 509, doi: [10.1086/373920](https://doi.org/10.1086/373920)

Guo, K., Ida, S., & Ogihara, M. 2025, arXiv e-prints, arXiv:2511.03246, doi: [10.48550/arXiv.2511.03246](https://doi.org/10.48550/arXiv.2511.03246)

Howard, A. W., Marcy, G. W., Johnson, J. A., et al. 2010, *Science*, 330, 653, doi: [10.1126/science.1194854](https://doi.org/10.1126/science.1194854)

Howard, A. W., Marcy, G. W., Bryson, S. T., et al. 2012, *ApJS*, 201, 15, doi: [10.1088/0067-0049/201/2/15](https://doi.org/10.1088/0067-0049/201/2/15)

Hut, P. 1981, *A&A*, 99, 126

Ida, S., & Lin, D. N. C. 2004, *ApJ*, 604, 388, doi: [10.1086/381724](https://doi.org/10.1086/381724)

Ida, S., Lin, D. N. C., & Nagasawa, M. 2013, *ApJ*, 775, 42, doi: [10.1088/0004-637X/775/1/42](https://doi.org/10.1088/0004-637X/775/1/42)

Kozai, Y. 1962, *AJ*, 67, 591, doi: [10.1086/108790](https://doi.org/10.1086/108790)

Lidov, M. L. 1962, *Planet. Space Sci.*, 9, 719, doi: [10.1016/0032-0633\(62\)90129-0](https://doi.org/10.1016/0032-0633(62)90129-0)

Lin, D. N. C., Bodenheimer, P., & Richardson, D. C. 1996, *Nature*, 380, 606, doi: [10.1038/380606a0](https://doi.org/10.1038/380606a0)

Lin, D. N. C., & Ida, S. 1997, *ApJ*, 477, 781, doi: [10.1086/303738](https://doi.org/10.1086/303738)

Liu, F., Asplund, M., Ramirez, I., Yong, D., & Melendez, J. 2014, *MNRAS*, 442, L51, doi: [10.1093/mnrasl/slu055](https://doi.org/10.1093/mnrasl/slu055)

Liu, S.-F., Agnor, C. B., Lin, D. N. C., & Li, S.-L. 2015, *MNRAS*, 446, 1685, doi: [10.1093/mnras/stu2205](https://doi.org/10.1093/mnras/stu2205)

Liu, S.-F., Guillochon, J., Lin, D. N. C., & Ramirez-Ruiz, E. 2013, *ApJ*, 762, 37, doi: [10.1088/0004-637X/762/1/37](https://doi.org/10.1088/0004-637X/762/1/37)

Liu, S.-F., Hori, Y., Müller, S., et al. 2019, *Nature*, 572, 355, doi: [10.1038/s41586-019-1470-2](https://doi.org/10.1038/s41586-019-1470-2)

Long, F., Herczeg, G. J., Harsono, D., et al. 2019, *ApJ*, 882, 49, doi: [10.3847/1538-4357/ab2d2d](https://doi.org/10.3847/1538-4357/ab2d2d)

Lucas, P. W., & Roche, P. F. 2000, *MNRAS*, 314, 858, doi: [10.1046/j.1365-8711.2000.03515.x](https://doi.org/10.1046/j.1365-8711.2000.03515.x)

Luhman, K. L. 2012, *ARA&A*, 50, 65, doi: [10.1146/annurev-astro-081811-125528](https://doi.org/10.1146/annurev-astro-081811-125528)

Ma, S., Mao, S., Ida, S., Zhu, W., & Lin, D. N. C. 2016, *MNRAS*, 461, L107, doi: [10.1093/mnrasl/slw110](https://doi.org/10.1093/mnrasl/slw110)

Malmberg, D., Davies, M. B., & Heggie, D. C. 2010, *Astronomy*, 22, 1

Matsumura, S., Ida, S., & Nagasawa, M. 2013, *ApJ*, 767, 129, doi: [10.1088/0004-637X/767/2/129](https://doi.org/10.1088/0004-637X/767/2/129)

Mayor, M. 2010, in *Exoplanets Rising: Astronomy and Planetary Science at the Crossroads*, 4

Mayor, M., Udry, S., Lovis, C., et al. 2009, *A&A*, 493, 639, doi: [10.1051/0004-6361:200810451](https://doi.org/10.1051/0004-6361:200810451)

Montet, B. T., Crepp, J. R., Johnson, J. A., Howard, A. W., & Marcy, G. W. 2014, *ApJ*, 781, 28, doi: [10.1088/0004-637X/781/1/28](https://doi.org/10.1088/0004-637X/781/1/28)

Mróz, P., Poleski, R., Gould, A., et al. 2020, *ApJL*, 903, L11, doi: [10.3847/2041-8213/abbfad](https://doi.org/10.3847/2041-8213/abbfad)

Mróz, P., Udalski, A., Skowron, J., et al. 2017, *Nature*, 548, 183, doi: [10.1038/nature23276](https://doi.org/10.1038/nature23276)

Murray, C. D., & Dermott, S. F. 1999, *Solar System Dynamics*, doi: [10.1017/CBO9781139174817](https://doi.org/10.1017/CBO9781139174817)

Nagasawa, M., & Ida, S. 2000, *AJ*, 120, 3311, doi: [10.1086/316856](https://doi.org/10.1086/316856)

—. 2011, *ApJ*, 742, 72, doi: [10.1088/0004-637X/742/2/72](https://doi.org/10.1088/0004-637X/742/2/72)

Nagasawa, M., Ida, S., & Bessho, T. 2008, *ApJ*, 678, 498, doi: [10.1086/529369](https://doi.org/10.1086/529369)

Nagasawa, M., Lin, D. N. C., & Ida, S. 2005, *ApJ*, 632, 1140, doi: [10.1086/433162](https://doi.org/10.1086/433162)

Nagasawa, M., Lin, D. N. C., & Ida, S. 2003, *ApJ*, 586, 1374, doi: [10.1086/367884](https://doi.org/10.1086/367884)

Nagasawa, M., Tanaka, H., & Ida, S. 2000, *AJ*, 119, 1480, doi: [10.1086/301246](https://doi.org/10.1086/301246)

Naoz, S. 2016, *ARA&A*, 54, 441, doi: [10.1146/annurev-astro-081915-023315](https://doi.org/10.1146/annurev-astro-081915-023315)

Oasa, Y., Tamura, M., & Sugitani, K. 1999, *ApJ*, 526, 336, doi: [10.1086/307964](https://doi.org/10.1086/307964)

Ochiai, H., Nagasawa, M., & Ida, S. 2014, *ApJ*, 790, 92, doi: [10.1088/0004-637X/790/2/92](https://doi.org/10.1088/0004-637X/790/2/92)

Offner, S. S. R., Moe, M., Kratter, K. M., et al. 2023, in *Astronomical Society of the Pacific Conference Series*, Vol. 534, *Protostars and Planets VII*, ed. S. Inutsuka, Y. Aikawa, T. Muto, K. Tomida, & M. Tamura, 275, doi: [10.48550/arXiv.2203.10066](https://doi.org/10.48550/arXiv.2203.10066)

Ogilvie, G. I. 2014, *Annual Review of Astronomy and Astrophysics*, 52, 171, doi: <https://doi.org/10.1146/annurev-astro-081913-035941>

Ogilvie, G. I., & Lin, D. N. C. 2004, *ApJ*, 610, 477, doi: [10.1086/421454](https://doi.org/10.1086/421454)

Pearson, S. G., & McCaughrean, M. J. 2023, arXiv e-prints, arXiv:2310.01231, doi: [10.48550/arXiv.2310.01231](https://doi.org/10.48550/arXiv.2310.01231)

Perryman, M. 2018, *The Exoplanet Handbook*

Rasio, F. A., & Ford, E. B. 1996, *Science*, 274, 954, doi: [10.1126/science.274.5289.954](https://doi.org/10.1126/science.274.5289.954)

Rein, H., & Liu, S.-F. 2011, 128, 1, doi: [10.1051/0004-6361/201118085](https://doi.org/10.1051/0004-6361/201118085)

Rein, H., & Spiegel, D. S. 2015, *MNRAS*, 446, 1424, doi: [10.1093/mnras/stu2164](https://doi.org/10.1093/mnras/stu2164)

Remus, F., Mathis, S., Zahn, J. P., & Lainey, V. 2012, *A&A*, 541, A165, doi: [10.1051/0004-6361/201118595](https://doi.org/10.1051/0004-6361/201118595)

Saffe, C., Jofré, E., Miquelarena, P., et al. 2019, *A&A*, 625, A39, doi: [10.1051/0004-6361/201935352](https://doi.org/10.1051/0004-6361/201935352)

Safronov, V. S. 1972, *Evolution of the protoplanetary cloud and formation of the earth and planets*.

Santerne, A., Moutou, C., Tsantaki, M., et al. 2016, *A&A*, 587, A64, doi: [10.1051/0004-6361/201527329](https://doi.org/10.1051/0004-6361/201527329)

Shen, Z. X., Jones, B., Lin, D. N. C., Liu, X. W., & Li, S. L. 2005, *ApJ*, 635, 608, doi: [10.1086/497264](https://doi.org/10.1086/497264)

Spurzem, R., Giersz, M., Heggie, D. C., & Lin, D. N. C. 2009, *ApJ*, 697, 458, doi: [10.1088/0004-637X/697/1/458](https://doi.org/10.1088/0004-637X/697/1/458)

Sridhar, S., & Tremaine, S. 1992, *Icarus*, 95, 86, doi: [10.1016/0019-1035\(92\)90193-B](https://doi.org/10.1016/0019-1035(92)90193-B)

Sumi, T., Kamiya, K., Bennett, D. P., et al. 2011, *Nature*, 473, 349, doi: [10.1038/nature10092](https://doi.org/10.1038/nature10092)

Sumi, T., Koshimoto, N., Bennett, D. P., et al. 2023, *AJ*, 166, 108, doi: [10.3847/1538-3881/ace688](https://doi.org/10.3847/1538-3881/ace688)

Tamayo, D., Rein, H., Shi, P., & Hernandez, D. M. 2020, *MNRAS*, 491, 2885, doi: [10.1093/mnras/stz2870](https://doi.org/10.1093/mnras/stz2870)

Tamura, M., Itoh, Y., Oasa, Y., & Nakajima, T. 1998, *Science*, 282, 1095, doi: [10.1126/science.282.5391.1095](https://doi.org/10.1126/science.282.5391.1095)

van Boekel, R., Henning, T., Menu, J., et al. 2017, *ApJ*, 837, 132, doi: [10.3847/1538-4357/aa5d68](https://doi.org/10.3847/1538-4357/aa5d68)

Veras, D., & Armitage, P. J. 2005, *ApJL*, 620, L111, doi: [10.1086/428831](https://doi.org/10.1086/428831)

von Zeipel, H. 1910, *Astronomische Nachrichten*, 183, 345, doi: [10.1002/asna.19091832202](https://doi.org/10.1002/asna.19091832202)

Wang, S., Kanagawa, K. D., & Suto, Y. 2022, *ApJ*, 932, 31, doi: [10.3847/1538-4357/ac68de](https://doi.org/10.3847/1538-4357/ac68de)

Weidenschilling, S. J., & Marzari, F. 1996, *Nature*, 384, 619, doi: [10.1038/384619a0](https://doi.org/10.1038/384619a0)

Wittenmyer, R. A., Wang, S., Horner, J., et al. 2020, *MNRAS*, 492, 377, doi: [10.1093/mnras/stz3436](https://doi.org/10.1093/mnras/stz3436)

Wu, Y., & Murray, N. 2003, *ApJ*, 589, 605, doi: [10.1086/374598](https://doi.org/10.1086/374598)

Zang, W., Jung, Y. K., Yee, J. C., et al. 2025, *Science*, 388, 400, doi: [10.1126/science.adn6088](https://doi.org/10.1126/science.adn6088)

Zhang, Y., & Lin, D. N. C. 2020, *Nature Astronomy*, 4, 852, doi: [10.1038/s41550-020-1065-8](https://doi.org/10.1038/s41550-020-1065-8)

Zheng, X., Kouwenhoven, M. B. N., & Wang, L. 2015, *MNRAS*, 453, 2759, doi: [10.1093/mnras/stv1832](https://doi.org/10.1093/mnras/stv1832)

Zheng, X., Lin, D. N. C., & Kouwenhoven, M. B. N. 2017a, *ApJ*, 836, 207, doi: [10.3847/1538-4357/836/2/207](https://doi.org/10.3847/1538-4357/836/2/207)

Zheng, X., Lin, D. N. C., Kouwenhoven, M. B. N., Mao, S., & Zhang, X. 2017b, *ApJ*, 849, 98, doi: [10.3847/1538-4357/aa8ef3](https://doi.org/10.3847/1538-4357/aa8ef3)

Zheng, X., Lin, D. N. C., & Mao, S. 2020, *ApJ*, 905, 169, doi: [10.3847/1538-4357/abc8e5](https://doi.org/10.3847/1538-4357/abc8e5)

—. 2021, *ApJ*, 914, 33, doi: [10.3847/1538-4357/abf5de](https://doi.org/10.3847/1538-4357/abf5de)

Zhou, J.-L., & Lin, D. N. C. 2007, *ApJ*, 666, 447, doi: [10.1086/520043](https://doi.org/10.1086/520043)

Zhou, J.-L., Lin, D. N. C., & Sun, Y.-S. 2007, *ApJ*, 666, 423, doi: [10.1086/519918](https://doi.org/10.1086/519918)

Zhu, W., & Dong, S. 2021a, *ARA&A*, 59, 291, doi: [10.1146/annurev-astro-112420-020055](https://doi.org/10.1146/annurev-astro-112420-020055)

—. 2021b, *ARA&A*, 59, 291, doi: [10.1146/annurev-astro-112420-020055](https://doi.org/10.1146/annurev-astro-112420-020055)

Zhu, W., & Wu, Y. 2018, *AJ*, 156, 92, doi: [10.3847/1538-3881/aad22a](https://doi.org/10.3847/1538-3881/aad22a)